

# Electronic Structure for Multielectronic Molecules near a Metal Surface

Published as part of *The Journal of Physical Chemistry virtual special issue "Emily A. Carter Festschrift"*.

Junhan Chen, Zuxin Jin, Wenjie Dou, and Joseph Subotnik\*



Cite This: *J. Phys. Chem. C* 2021, 125, 2884–2899



Read Online

ACCESS |



Metrics & More

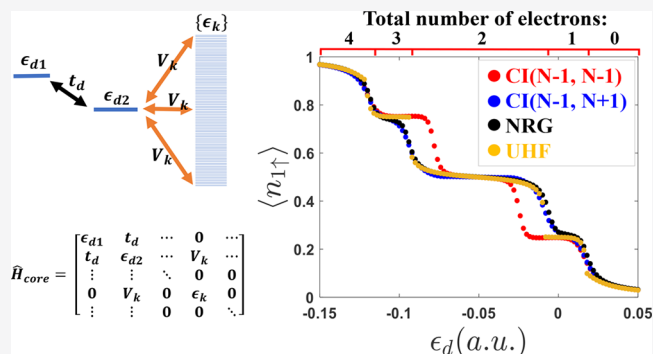


Article Recommendations



Supporting Information

**ABSTRACT:** We analyze a model problem representing a multielectronic molecule sitting on a metal surface. Working with a reduced configuration interaction Hamiltonian, we show that one can extract very accurate ground state wave functions as compared with numerical renormalization group theory (NRG)—even in the limit of weak metal–molecule coupling strength but strong intramolecular electron–electron repulsion. Moreover, we extract what appear to be meaningful excitation energies as well. Our findings should lay the groundwork for future *ab initio* studies of charge transfer processes and bond making/breaking processes on metal surfaces.



## I. INTRODUCTION

Understanding the metal–molecule interface is essential for understanding heterogeneous catalysis. In order to understand macroscopically why heterogeneous catalysts enhance reaction rates and improve production yield, we require a microscopic understanding of chemical reactions on an atomic scale. To that end, developing robust and atomistic quantum models of molecular processes that occur on metal surfaces, including electron-coupled adsorption<sup>1</sup> and electron-coupled vibration,<sup>2,3</sup> is an important goal for modern theory. And in order to achieve such a goal, at least within the standard Born–Oppenheimer framework, the very first step is to solve the interfacial electronic structure problem. If we can calculate potential energies that are accurate enough, then a host of dynamical approaches for the nuclear problem (Marcus theory<sup>4</sup> and beyond<sup>5–8</sup>) will be applicable, and new dynamical techniques are still being developed.<sup>9–12</sup>

Unfortunately, solving electronic structure problems is a very difficult task (in general), even for isolated molecules in the gas phase. As is well-known, Hartree–Fock (HF) calculations show large discrepancies with experimental results even for isolated molecules:<sup>13</sup> the H + H<sub>2</sub> reaction barrier,<sup>14,15</sup> the dissociation energy for hydrogen fluoride,<sup>16,17</sup> the ionization potential,<sup>18,19</sup> and the electron affinity<sup>20,21</sup> of the oxygen atom. Thus, even for small molecules, electron–electron correlation is important and of course expensive, scaling exponentially with the number of electrons. For large molecules, the situation is worse: one recent photochemistry study revealed that a correct treatment of electron correlation is needed to find the correct open-shell radical products (instead of closed-shell singlet products) in the

case of a bond-breaking reaction with carbenes and biradicals.<sup>22</sup> Obviously, an accurate treatment of electronic correlation is essential for theory to match experiments even in the gas phase.

Now, if the state of affairs above (vis-à-vis electronic correlation for molecules in the gas phase) is unfortunate, the state of affairs in condensed matter physics is even worse. In the solid world, on-site electron–electron repulsion can result in metal–insulator transitions for narrow energy bands, e.g., the d-band in transition metals<sup>23</sup> and half-filling magic-angle graphene.<sup>24</sup> Within a solid, the electron correlation problem can couple together electronic states that are far apart not only in energy but also in space, and perturbative treatments of electron correlation will often not be helpful. In the end, the computational cost needed to accurately solve the electronic structure problem in the condensed phase becomes simply immense and is motivating an enormous push today within the physics community.<sup>25–29</sup>

With this background in mind, the theory of interfacial electronic structure (i.e., electronic structure for molecules on metal surfaces) lies somewhere in between the two extreme limits above. On the one hand, the interfacial problem has all of the difficulties described above as far as the electronic structure

Received: September 27, 2020

Revised: December 3, 2020

Published: January 28, 2021



calculations of molecules. To accurately describe a molecule on a metal surface, we require a sufficient treatment of static correlation (to describe bond breaking) as well as a sufficient treatment of dynamical correlation (to describe accurate, molecular orbital energies). Moreover, when describing dynamic correlation, one must also take into account the orbital energies on the metal. On the other hand, however, the interfacial electronic structure is easier than the condensed phase problem insofar as the fact that one can focus most of his/her attention on the molecule. For the most part, the static correlation problem is localized in space on the molecule (even if the dynamic correlation problem is spread out over the molecule and the metal). To describe correlation in solids, one typically follows Fermi liquid theory and uses DFT or some other effective mean-field theory. As a result, the interfacial problem is effectively an impurity problem, for which there is a significant literature going back to the original Anderson model of a localized magnetic state in a sea of metallic electrons.<sup>30</sup> The simplest one-site Anderson impurity model has been studied by a variety of impurity solvers including numerical renormalization group (NRG),<sup>31</sup> exact diagonalization (ED)<sup>32</sup> and quantum Monte Carlo (QMC).<sup>33</sup> More generally, solving the embedding problem in quantum chemistry has attracted a great deal of attention in recent years.<sup>29,34–40</sup>

For our purposes, we are interested in coupled nuclear–electronic processes that occur at metal–molecule interfaces, especially electron transfer processes and bond making or breaking processes. For such processes, with two stable configurations (e.g., donor and acceptor), we can certainly expect that static correlation effects will be essential, and one must go beyond mean-field theories.<sup>41</sup> Within the quantum chemistry community, this line of thinking leads to different techniques in the literature.

1. For processes that involve the charge character of the system, constrained DFT (CDFT)<sup>42,43</sup> is perhaps the simplest means to generate diabatic states and charge transfer excited states. This technique works extremely well in the limit of weak coupling (e.g., O<sub>2</sub> on Al(111)<sup>44</sup> and benzene on Li(100)<sup>45</sup>) but shows larger errors for strong coupling (e.g., N<sub>2</sub> on Ni(001)<sup>46</sup>).
2. Beyond CDFT, there is of course a natural hierarchy of increasingly expensive wave function techniques, including multireference configuration interaction (MRCI) methods and/or multiconfigurational self-consistent field (MCSCF). In particular, for problems with static correlation, the methods of choice today remain complete active space (CAS)<sup>47,48</sup> methods. According to the definition of CAS, one usually chooses valence orbitals as the active space and the remaining inactive space refers to those orbitals which are either always occupied or always unoccupied. Here, a CAS(*N*,*m*,*S*) represents *N* active electrons in *m* active orbitals with total spin quantum number *S* (strictly speaking, *S* is equal to one-half of the number of singly occupied orbitals). The number of configurations contained in a MCSCF wave function is given by the Weyl–Robinson formula:<sup>48,49</sup>

$$\frac{2S+1}{m+1} \binom{m+1}{m-\frac{N}{2}-S} \binom{m+1}{\frac{N}{2}-S} \quad (1)$$

When *N* and *m* are small, CAS methods are accurate and fast. However, for larger molecules, with finite speed and

memory capabilities, one cannot afford to include very many orbitals in the active space of a CASSCF calculation—even with advanced bookkeeping techniques.<sup>50</sup> Moreover, due to the exponential scaling of the number of Slater determinants with the number of orbitals and electrons, the practical upper limit for CAS is about 24 electrons in 24 active orbitals.<sup>51</sup> (In the context of the density matrix renormalization group (DMRG) algorithm, the number of active orbitals can go as large as 100.<sup>52</sup>) As a result, for accurate energies, within the molecular community, one tries (if possible) to include dynamical correlation either by calculating a second-order perturbation correction (MR-PT, e.g. CASPT2<sup>53</sup>), solving a configuration interaction (CI) problem with MCSCF wave functions as the reference states (e.g., CAS(2,2)CISD<sup>54</sup>), or even solving for a multireference couple-cluster solution (MR-CC, e.g. ACPF<sup>55</sup>).

3. Finally, historically, there have also been attempts to merge DFT with CI to recover the multiconfigurational character for *molecules*, stretching back to the early work of Clementi, San-Fabian, Savin, Grimme, and co-workers.<sup>56–64</sup> The overall question that must be addressed is how to merge a local DFT dynamic correlation correction with a configuration interaction (usually active space) model that treats static correlation. One must choose orbitals, one must choose functionals, and many options are possible in principle. In recent years, Pijeu and Hohenstein<sup>65</sup> have suggested (with some success) merging DFT with CASCI by replacing the HF core energy with a DFT core energy. Gagliardi, Truhlar and co-workers<sup>66–69</sup> have perhaps had the strongest impact with their “multiconfiguration pair-density functional theory” (MC-PDFT), whereby one simply includes an exchange–correlation function in terms of the one-body density and the two-body density that are generated from a CAS calculation.<sup>61</sup>

To our knowledge, of all the methods listed above, only CDFT has been applied to a realistic metal surface, with varying degrees of success.<sup>42–45</sup> For the truly multiconfigurational approaches, the computational cost is enormous and these techniques are not readily used to study interfacial electronic structure (though see recent work of Levine et al. for an interesting CAS calculation of dangling bonds on a silicon cluster).<sup>70</sup>

At this point, it should be clear to the reader that strong approximations will be necessary in order to practically and robustly solve for the electronic structure of a molecule reacting on a metal surface, while capturing enough correlation energy for even qualitative (and ideally quantitative) accuracy. In order to achieve such a goal, in this paper, we will follow a three-pronged approach. First, we will run a standard SCF/DFT calculation to allow for electrons to be delocalized; second, we will use a projection technique, which is similar to the framework of Chan’s density matrix embedding theory (DMET),<sup>34</sup> to generate molecular orbitals corresponding to a molecule on a metal surface; third, we will generate and diagonalize a configuration interaction Hamiltonian that will allow for multireference behavior while also yielding information about excited states. For the present paper, we will restrict ourselves to a two-site impurity with electron repulsion (representing a molecule) coupled to a set of noninteracting Fermions (representing a metal bath)—but in the future, we intend to

apply the present approach to *ab initio* (rather than model) calculations. For now, though, in order to make sure that we recover accurate results for a model problem, we will compare all of our configuration interaction data against (exact) numerical renormalization group theory (NRG),<sup>51</sup> which is expensive but possible for a small model Hamiltonian. In the end, our hope is that the present methodology (or some variant) should allow us to model accurately the dynamics of molecular charge transfer, bond-making, or bond-breaking processes on a metal surface.

This paper is organized as follows. In Section II, we introduce the two-site Anderson impurity Hamiltonian, which will serve as our model Hamiltonian (representing a many-electron molecule sitting on a metal surface). We further introduce the necessary projection operators that are needed for constructing (effectively) an embedded set of orbitals on the impurity that interacts with a metal surface. In Section II.E, using the molecular orbitals just defined, we introduce a host of configuration interaction methods for approximating the total Hamiltonian (molecule plus metal). In Section III, we present results, demonstrating that for many parameter regimes, one can invoke (with accuracy) a CI technique we label CI( $N-1, N-1$ ), which includes  $N-1$  singly excited configurations plus  $N-1$  doubly excited configurations in total. In Section IV, we further analyze our data and, in particular, we investigate the regime whereby one appears to break a molecular bond on the metal surface. For this parameter regime, we find that achieving accuracy requires at least two more doubly excited configurations (leading to a CI( $N-1, N+1$ ) ansatz), whose meaning we discuss in detail. In Section V, we summarize our findings and give an outlook for prospective future applications with realistic *ab initio* systems.

A word about notation is now appropriate and essential. Henceforward, we will refer to “impurities” when discussing a molecule (sitting on a metal surface) and we will refer to a “bath” when discussing the metal. The term “universe” will denote the impurity plus the metal. When performing electronic structure calculations, many different sets of orbitals can and will be constructed. In what follows below, we will represent the underlying atomic orbital basis for our calculation as  $\{|\chi_\nu\rangle\}$ , where  $\nu$  runs over all sites in the universe. We will represent the canonical Kohn–Sham or HF orbitals (which are delocalized over both the impurity and the metal bath) as  $\{|\tilde{\psi}_i\rangle\}$ . Greek indices ( $\mu, \nu$ ) strictly index atomic sites, whereas roman indices index delocalized orbitals. As usual,  $i, j, k$  index occupied delocalized orbitals, whereas  $a, b, c$  index virtual delocalized orbitals. The calculation below will rely on the construction of impurity-projected occupied orbitals (IPOOs) and impurity-projected virtual orbitals (IPVOs), which are referenced (respectively) as  $|\phi_\nu^{occ}\rangle$  and  $|\phi_\nu^{virt}\rangle$ . Finally, the most important set of orbitals constructed below will be those orbitals that span the occupied canonical space, but have been separated into impurity and bath components; these orbitals will be labeled  $\{|\psi_1\rangle, |\psi_2\rangle, \dots, |\psi_{n-1}\rangle, |\psi_n\rangle\}$ . Similarly orbitals will also be constructed for the virtual space:  $\{|\psi_1\rangle, |\psi_{i+1}\rangle, \dots, |\psi_N\rangle\}$ .<sup>71</sup> Finally, throughout this manuscript, we will attempt to avoid using the common phrase “molecular orbitals”, which could easily refer to several of the orbital sets listed above.

## II. THEORY

**II.A. Two-Site Anderson Impurity Model.** For the present manuscript, our model Hamiltonian of choice will be the two-site Anderson impurity model (AIM). Within a second

quantized representation, the Hamiltonian for the universe can be written as

$$\begin{aligned} \hat{H} = & \epsilon_d \sum_{\sigma} d_{1\sigma}^{\dagger} d_{1\sigma} + (\epsilon_d + \Delta\epsilon_d) \sum_{\sigma} d_{2\sigma}^{\dagger} d_{2\sigma} \\ & + t_d \sum_{\sigma} (d_{1\sigma}^{\dagger} d_{2\sigma} + d_{2\sigma}^{\dagger} d_{1\sigma}) + U(d_{1\uparrow}^{\dagger} d_{1\downarrow}^{\dagger} d_{1\downarrow} \\ & + d_{2\uparrow}^{\dagger} d_{2\downarrow}^{\dagger} d_{2\downarrow}) + \sum_{k\sigma} \epsilon_{k\sigma} c_{k\sigma}^{\dagger} c_{k\sigma} \\ & + \sum_{k\sigma} V_k (d_{1\sigma}^{\dagger} c_{k\sigma} + c_{k\sigma}^{\dagger} d_{1\sigma}) \end{aligned} \quad (2)$$

The universe’s Hamiltonian can be separated into two parts: the one-electron core Hamiltonian and the two-electron term:

$$\hat{H} \equiv \hat{H}_{core} + \hat{\Pi} \quad (3)$$

where,

$$\begin{aligned} \hat{H}_{core} = & \epsilon_d \sum_{\sigma} d_{1\sigma}^{\dagger} d_{1\sigma} + (\epsilon_d + \Delta\epsilon_d) \sum_{\sigma} d_{2\sigma}^{\dagger} d_{2\sigma} \\ & + t_d \sum_{\sigma} (d_{1\sigma}^{\dagger} d_{2\sigma} + d_{2\sigma}^{\dagger} d_{1\sigma}) + \sum_{k\sigma} \epsilon_{k\sigma} c_{k\sigma}^{\dagger} c_{k\sigma} \\ & + \sum_{k\sigma} V_k (d_{1\sigma}^{\dagger} c_{k\sigma} + c_{k\sigma}^{\dagger} d_{1\sigma}) \end{aligned} \quad (4)$$

$$\hat{\Pi} = U(d_{1\uparrow}^{\dagger} d_{1\downarrow}^{\dagger} d_{1\downarrow} + d_{2\uparrow}^{\dagger} d_{2\downarrow}^{\dagger} d_{2\downarrow}) \quad (5)$$

This Hamiltonian can be visualized as in Figure 1. The creation and annihilation operators  $\{\hat{d}^{\dagger}, \hat{d}\}$  refer to impurity

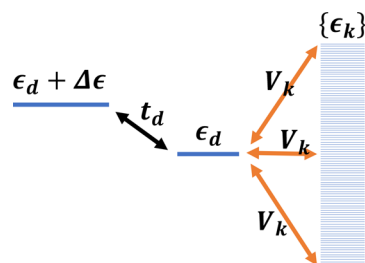


**Figure 1.** Schematic figure for the two-site Anderson impurity Hamiltonian.

atomic orbitals (which should represent a molecule on a surface), the operators  $\{\hat{c}^{\dagger}, \hat{c}\}$  refer to bath (metal surface) atomic orbitals, and  $\sigma$  refers to an electron spin.  $\epsilon_d$  and  $\epsilon_d + \Delta\epsilon_d$  are ionization energies for impurity site 1 and site 2.  $t_d$  is the hopping parameter between site 1 and site 2,  $U$  represents the on-site coulomb repulsion for the impurity.  $\epsilon_k$  represents the energy of the free-electron metallic orbital with momentum  $k$ , while  $V_k$  represents the hybridization between impurity site 1 and the metal bath.<sup>72</sup>

For all of our calculations below, we will make the wide-band approximation; i.e., we assume the hybridization width  $\Gamma(\epsilon) = 2\pi \sum_k |V_k|^2 \delta(\epsilon - \epsilon_k) = \Gamma$  is independent of energy. In practice, we enforce this assumption by assuming that both  $V_k$  and the density of states  $\rho(\epsilon)$  are constants (that do not depend on the bath index  $k$ ). We have made this approximation so that we will be able to easily compare our results with (exact) numerical renormalization group theory (NRG) results. For all calculations below, we set  $\Gamma = 0.01$  hartree,  $U = 10\Gamma = 0.1$  hartree and the bandwidth for the bath  $W = 0.8$  hartree, ranging from  $-0.4$  to  $+0.4$  hartree. A total of 800 bath states are evenly distributed

inside this energy window so that the energy spacing for the bath states is  $\Delta E = 0.001$  (i.e., the density of the bath states is  $\rho(\epsilon) = 1000$ ). Extending the present model to go beyond the wide band approximation (with nonconstant  $\Gamma$ ) should be straightforward; indeed, we already have some results for a tight-binding Hamiltonian.

**II.B. Choosing an Orbital Active Space for the Molecular Impurity.** In order to build up a configuration interaction Hamiltonian for a molecular impurity on a metal surface, we will require a set of impurity orbitals that we can associate as belonging to the impurity. Although many projection schemes have been developed over the past several years,<sup>34,73</sup> we will choose an approach similar to the projected Wannier functions algorithm.<sup>74</sup>

We begin by performing a standard mean-field theory (MFT) calculation. The resulting MFT eigenstates  $\{|\tilde{\psi}_p\rangle\}$  are delocalized wave functions and come in two flavors: occupied and virtual. The projection operators for each subspace are  $\hat{P}_{occ}$  and  $\hat{P}_{virt}$ :

$$\hat{P}_{occ} = \sum_{i \in occ} |\tilde{\psi}_i\rangle\langle\tilde{\psi}_i| \quad (6)$$

$$\hat{P}_{virt} = \hat{I} - \hat{P}_{occ} = \sum_{a \in virt} |\tilde{\psi}_a\rangle\langle\tilde{\psi}_a| \quad (7)$$

Next, we project the impurity atomic orbitals  $\{|\chi_\nu\rangle\}_{\nu=1,2}^{imp}$  into the occupied and virtual subspaces as follows:

$$|\chi_\nu\rangle^{imp} = \frac{\hat{P}_{occ}|\chi_\nu\rangle^{imp}}{|\tilde{\phi}_\nu^{occ}\rangle} + \frac{\hat{P}_{virt}|\chi_\nu\rangle^{imp}}{|\tilde{\phi}_\nu^{virt}\rangle} \quad (8)$$

Here, the projected functions are

$$|\tilde{\phi}_\nu^{occ}\rangle = \sum_{i \in occ} |\tilde{\psi}_i\rangle\langle\tilde{\psi}_i|\chi_\nu\rangle^{imp}$$

$$|\tilde{\phi}_\nu^{virt}\rangle = \sum_{a \in virt} |\tilde{\psi}_a\rangle\langle\tilde{\psi}_a|\chi_\nu\rangle^{imp}$$

Note that, if we had a more complicated Hamiltonian representing a larger molecular system, we would have more than two atomic sites—and yet the present formalism can be extended in an obvious fashion.

Lastly, the projected orbitals  $\{|\tilde{\phi}_\nu^{occ}\rangle\}_{\nu=1,2}$  and  $\{|\tilde{\phi}_\nu^{virt}\rangle\}_{\nu=1,2}$  are orthogonal in the sense that all occupied and virtual basis functions satisfy:  $\langle\tilde{\phi}_\mu^{occ}|\tilde{\phi}_\nu^{virt}\rangle = 0$ . However, these functions are not orthogonal in the sense that  $\langle\tilde{\phi}_\mu^{occ}|\tilde{\phi}_\nu^{occ}\rangle \neq \delta_{\mu\nu}$  and  $\langle\tilde{\phi}_\mu^{virt}|\tilde{\phi}_\nu^{virt}\rangle \neq \delta_{\mu\nu}$ . Nevertheless, one can easily recover an orthonormal basis by performing a Löwdin orthogonalization,<sup>50</sup> yielding  $\{|\phi_\nu^{occ}\rangle\}_{\nu=1,2}$  and  $\{|\phi_\nu^{virt}\rangle\}_{\nu=1,2}$ .

The steps above can be summarized mathematically (in the precise language of ref 74) as follows:

1. Compute a matrix of inner products  $(A_{occ})_{iv} = \langle\tilde{\psi}_i|\chi_\nu\rangle^{imp}$ . Then the projection can be written as

$$|\tilde{\phi}_\nu^{occ}\rangle = \sum_{i \in occ} |\tilde{\psi}_i\rangle(A_{occ})_{iv} \quad (9)$$

2. Compute the overlap matrix  $(S_{occ})_{\mu\nu} = (A_{occ}^\dagger A_{occ})_{\mu\nu}$
3. Construct the Löwdin-orthogonalized impurity-projected occupied orbitals (IPOOs):

$$\begin{aligned} |\phi_\nu^{occ}\rangle &= \sum_{\mu} |\tilde{\phi}_\mu^{occ}\rangle(S_{occ}^{-1/2})_{\mu\nu} \\ &= \sum_{i \in occ} |\tilde{\psi}_i\rangle(A_{occ}S_{occ}^{-1/2})_{iv} \end{aligned} \quad (10)$$

4. A similar construction is applied for the virtual space to generate impurity-projected virtual orbitals (IPVOs).

Note that the quantity  $A_{occ}S_{occ}^{-1/2}$  in eq 10 is a unitary transformation. After all, according to a singular value decomposition,

$$\begin{aligned} (A_{occ})_{kv} &= \sum_{p=1}^2 U_{kp}\lambda_p V_{pv}^\dagger \\ (S_{occ})_{\mu\nu} &= (A_{occ}^\dagger A_{occ})_{\mu\nu} = \sum_{p=1}^2 V_{\mu p}\lambda_p^2 V_{p\nu}^\dagger \\ &\rightarrow A_{occ}S_{occ}^{-1/2} = UV^\dagger \end{aligned}$$

**II.C. Constructing Frontier Orbitals by Minimization of the Energy of a Double Excitation.** The IPOOs  $\{|\phi_\nu^{occ}\rangle\}_{\nu=1,2}$  and IPVOs  $\{|\phi_\nu^{virt}\rangle\}_{\nu=1,2}$  form an active subspace of orbitals for the impurity within the context of the two-site Hamiltonian considered here. More generally, one would like to work with impurities (or really molecules) with many, many electrons. And so, in order to make progress with any form of electron–electron correlation, we will need to construct HOMO and LUMO orbitals for the impurity. To that end, we will roughly follow the approach in ref 75. This approach can be made very clear (and explicit) using the current simple model, with only two sites.

We begin by rotating the projected orbitals:

$$\begin{aligned} (|\psi_{h-1}\rangle|\psi_h\rangle) &= (|\phi_1^{occ}\rangle|\phi_2^{occ}\rangle) \begin{pmatrix} -\sin(\theta_1) & \cos(\theta_1) \\ \cos(\theta_1) & \sin(\theta_1) \end{pmatrix} \\ (|\psi_l\rangle|\psi_{l+1}\rangle) &= (|\phi_1^{virt}\rangle|\phi_2^{virt}\rangle) \begin{pmatrix} \cos(\theta_2) & -\sin(\theta_2) \\ \sin(\theta_2) & \cos(\theta_2) \end{pmatrix} \end{aligned}$$

The premise of ref 75 is to pick the angles  $\theta_1$  and  $\theta_2$  above (and hence optimized orbitals  $\{|\psi_{h-1}\rangle, |\psi_h\rangle\}$  and  $\{|\psi_l\rangle, |\psi_{l+1}\rangle\}$ ) by minimizing the energy for the doubly excited configuration:  $|\Psi_{hh}^{ll}\rangle$ . Explicitly, the energy for this doubly excited configuration is (assuming a closed-shell restricted set of orbitals):

$$\begin{aligned} E_{double} &= 2\text{tr}(\hat{H}_{core}\hat{P}_{occ}) - 2\langle\psi_h|\hat{H}_{core}|\psi_h\rangle + 2\langle\psi_l|\hat{H}_{core}|\psi_l\rangle \\ &+ U[(\langle\hat{n}_1\rangle - \langle\psi_h|\hat{n}_1|\psi_h\rangle + \langle\psi_l|\hat{n}_1|\psi_l\rangle)^2 \\ &+ (\langle\hat{n}_2\rangle - \langle\psi_h|\hat{n}_2|\psi_h\rangle + \langle\psi_l|\hat{n}_2|\psi_l\rangle)^2] = E_{HF} - 2F_{hh} \\ &+ 2F_{ll} + U(\langle\psi_h|\hat{n}_1|\psi_h\rangle - \langle\psi_l|\hat{n}_1|\psi_l\rangle)^2 + U \\ &(\langle\psi_h|\hat{n}_2|\psi_h\rangle - \langle\psi_l|\hat{n}_2|\psi_l\rangle)^2 \end{aligned} \quad (11)$$

Here,  $E_{HF}$  is the Hartree–Fock ground state energy

$$E_{HF} = 2\text{tr}(\hat{H}_{core}\hat{P}_{occ}) + U(\langle\hat{n}_1\rangle^2 + \langle\hat{n}_2\rangle^2) \quad (12)$$

$\hat{H}_{core}$  is the one-electron term in eq 4 and  $\hat{F}$  is the fock operator as constructed by a standard HF calculation:

$$\hat{F} = \hat{H}_{core} + U(\hat{n}_1\langle\hat{n}_1\rangle + \hat{n}_2\langle\hat{n}_2\rangle) \quad (13)$$

Finally,  $F_{hh} \equiv \langle\psi_h|\hat{F}|\psi_h\rangle$  and  $F_{ll} \equiv \langle\psi_l|\hat{F}|\psi_l\rangle$ .

Table 1. Selective CI Calculations<sup>a</sup>

Methods*	Configurations**	Number of Configurations (N=803, N <sub>o</sub> =400, N <sub>v</sub> =403)
CAS(2,2)	$ \Phi_{HF}\rangle,  S_h^t\rangle,  \Phi_{hh}^{\bar{t}}\rangle$	3
CI(N-1,1)	$ \Phi_{HF}\rangle,  S_i^t\rangle,  S_h^a\rangle,  \Phi_{hh}^{\bar{t}}\rangle$	N+1 (804)
CI(1,N-1)	$ \Phi_{HF}\rangle,  S_h^t\rangle,  ^1\Phi_{ih}^t\rangle,  ^1\Phi_{hh}^a\rangle$	N+1 (804)
CI(N-1,N-1)	$ \Phi_{HF}\rangle,  S_i^t\rangle,  S_h^a\rangle,  ^1\Phi_{ih}^t\rangle,  ^1\Phi_{hh}^a\rangle$	2N-1 (1605)
CI(N-1,N+1)	$ \Phi_{HF}\rangle,  S_i^t\rangle,  S_h^a\rangle,  ^1\Phi_{ih}^t\rangle,  ^1\Phi_{hh}^a\rangle,  \Phi_{h-1h-1}^{\bar{t}}\rangle,  \Phi_{hh}^{t+M+1}\rangle$	2N+1 (1607)
CI(N <sub>ov</sub> ,1)	$ \Phi_{HF}\rangle,  S_i^b\rangle,  \Phi_{hh}^{\bar{t}}\rangle$	N <sub>o</sub> N <sub>v</sub> +2 (161202)
MRCIS	$ \Phi_{HF}\rangle,  S_i^b\rangle,  D_{hh}^b\rangle_A,  D_{hh}^b\rangle_B,  T_{hh}^a\rangle$	4N <sub>o</sub> N <sub>v</sub> -2N <sub>o</sub> -2N <sub>v</sub> +3 (643197)

<sup>a</sup>Key: \*CI(X,Y) represents X number of singly excited configurations and Y number of doubly excited configurations, N is the total number of orbitals, including N<sub>o</sub> number of occupied orbitals and N<sub>v</sub> number of virtual orbitals. \*\*Singlet spin-adapted configurations.

**II.D. Putting It All Together: A Complete Basis That Extrapolates The Optimized Orbitals.** Having constructed  $\{|\psi_{h-1}\rangle, |\psi_h\rangle\}$ , we can extend this two-dimensional set of vectors to include  $N_{occ} - 2$  more functions so as to form a complete basis for the occupied space. To do this in the most numerically stable fashion, we construct  $\{|\psi_i\rangle\}_{i=1, \dots, N_{occ}-2}$  (which label the bath) according to a standard canonical orthogonalization procedure.<sup>50</sup> Namely, we first calculate the projector onto the reduced occupied space:

$$S = \hat{P}_{occ} - |\psi_{h-1}\rangle\langle\psi_{h-1}| - |\psi_h\rangle\langle\psi_h| \quad (14)$$

Next, we express S in the basis of atomic orbitals ( $N \times N$ ) and then diagonalize it:

$$s = V'SV \quad (15)$$

If everything above is completely stable numerically, we should find that S has  $N_{vir} + 2$  zero eigenvalues. And even if numerical instabilities arise, we can always just sort the resulting eigenvalues in descending order. In the end, we can generate a coefficient matrix  $\tilde{X}$ :

$$\tilde{X} = \begin{bmatrix} V_{1,1}/s_1^{1/2} & V_{1,2}/s_2^{1/2} & \dots & V_{1,N_o-2}/s_{N_o-2}^{1/2} \\ V_{2,1}/s_1^{1/2} & V_{2,2}/s_2^{1/2} & \dots & V_{2,N_o-2}/s_{N_o-2}^{1/2} \\ \vdots & \vdots & \ddots & \vdots \\ V_{N,1}/s_1^{1/2} & V_{N,2}/s_2^{1/2} & \dots & V_{N,N_o-2}/s_{N_o-2}^{1/2} \end{bmatrix} \quad (16)$$

that gives us a prescription for the complete occupied space:

$$|\psi_i\rangle = \sum_{\nu} |\chi_{\nu}\rangle \tilde{X}_{\nu i}, \quad i = 1, 2, \dots, N_o - 2 \quad (17)$$

, where  $\{|\chi_{\nu}\rangle\}$  are atomic orbitals. Note that the  $\sqrt{s_i}$  factors in the denominators on the right-hand side of eq 16 are included only to normalize the  $\{|\psi_i\rangle\}$  functions.

In the end, the take-away message from this entire section is that we have constructed a complete set of occupied orbitals ( $|\psi_1\rangle, |\psi_2\rangle, \dots, |\psi_{h-1}\rangle, |\psi_h\rangle$ ) whereby  $|\psi_{h-1}\rangle$  and  $|\psi_h\rangle$  can be associated with the impurity, and all other orbitals are associated with the bath. Of course, the same procedure can be done for the virtual space (where now we work with  $|\psi_i\rangle$  and  $|\psi_{i+1}\rangle$  instead of  $|\psi_{h-1}\rangle$  and  $|\psi_h\rangle$ ). Henceforward, in the spirit of DMET,<sup>34</sup> we will call these two sets of orbitals  $\{|\psi_{h-1}\rangle, |\psi_h\rangle\}$  and  $\{|\psi_i\rangle, |\psi_{i+1}\rangle\}$  occupied entangled orbitals (OEOs) and virtual entangled orbitals (VEOs), respectively. We will refer to the remaining two sets of orbitals  $\{|\psi_1\rangle, |\psi_2\rangle, \dots, |\psi_{h-2}\rangle\}$  and  $\{|\psi_{h+2}\rangle, \dots, |\psi_N\rangle\}$  as

occupied bath orbitals (OBOs) and virtual bath orbitals (VBOs), respectively.

**II.E. Selecting a Configuration Interaction Basis.** The goal of this paper is to establish and compare a set of different configuration interaction methods for capturing the electronic structure of an impurity on a metal surface. To that end, in Table 1, we list seven possible CI ansätze that will appear natural to the seasoned quantum chemist/physicist. Our notation is as follows:

- CAS(2,2) [Complete Active Space(2,2)] represents all configurations with 2 electrons on 2 orbitals  $\{|\psi_h\rangle, |\psi_i\rangle\}$ .
- CI(X,Y) represents a selective configuration interaction Hamiltonian with only single and double excitations: X is the number of singly excited configuration and Y is the number of doubly excited configuration.

Now, obviously, the notation CI(X,Y) is not unique: which X single and which Y double excitations should we include? Thus, in Table 1, in the middle column, we list explicitly the configurations. For example, CI(N<sub>ov</sub>,1) includes  $N_o \times N_v$  singly excited configurations and one doubly excited configuration (which we called "CIS-1D" in ref 75). To better understand this table, note the following nomenclature conventions we have used:

1.  $\{|\Phi_{HF}\rangle\}$  denotes the Hartree–Fock ground state.
2. The subscript *i* indexes all occupied orbitals, including occupied entangled orbitals  $\{|\psi_{h-1}\rangle, |\psi_h\rangle\}$  and occupied bath orbitals.
3. The subscript *a* includes the virtual entangled orbital  $\{|\psi_{i+1}\rangle\}$  and all virtual bath orbitals, but excludes the virtual entangled orbital  $\{|\psi_i\rangle\}$  (in order to avoid double counting ( $|S_h^{a-1}\rangle = |S_{i=h}^a\rangle$ )).
4. The subscript *b* in CI(N<sub>ov</sub>,1) denotes all unoccupied orbitals, associate or not associated with the impurity.
5. Every configuration is a singlet spin-adapted configuration:  $|S_h^t\rangle = \frac{1}{\sqrt{2}}(|\Phi_h^t\rangle + |\Phi_h^{\bar{t}}\rangle)$  and  $|^1\Phi_{ih}^t\rangle = \frac{1}{\sqrt{2}}(|\Phi_{ih}^{\bar{t}}\rangle + |\Phi_{ih}^t\rangle)$ . For the case  $i = h$ , we set  $|^1\Phi_{ih}^t\rangle = |\Phi_{hh}^{\bar{t}}\rangle$ .

On the right-hand side of Table 1, we list the total number of configurations for each approach. Here, N denotes the total orbitals, including N<sub>o</sub> occupied orbitals and N<sub>v</sub> virtual orbitals. As should be clear from the description above, we have constructed two occupied orbitals associated with the impurity, N<sub>o</sub> - 2 occupied orbitals associated with the bath, two virtual orbitals associated with the impurity, and N<sub>v</sub> - 2 virtual orbitals associated with the bath; see Figure 2.

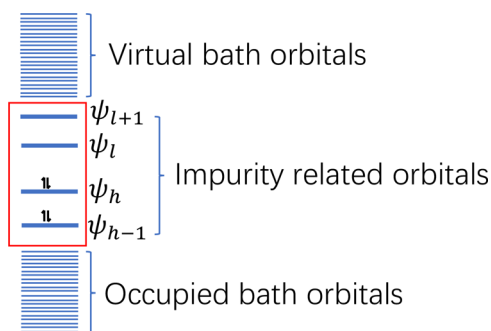


Figure 2. Schematic figure of the relevant orbitals.<sup>76</sup>

Note that, for the most part, our choice of CI subspaces does not correspond to any particular restricted active space. In particular, because of the need to account for charge transfer between molecule and metal, combined with the presence of so many metallic orbitals, a meaningful restricted active space model [beyond the CAS(2,2) space] would be very large and expensive. Thus, in order to include enough configurations of relevance to the impurity, our approach has been to start with the HF state and include single or double excitation on top of this single-state reference. The only exception to this rule is our inclusion of the MRCIS method in Table 1, which includes all single excitations on top of the three electronic states in a CAS(2,2) calculation; the MRCIS method is by far the largest and most expensive CI method we investigate here. In Table 1, we use the singlet spin-adapted configuration:

1. Single excitation:  $|S_i^b\rangle = \frac{1}{\sqrt{2}}(|\Phi_i^b\rangle + |\Phi_{\bar{i}}^{\bar{b}}\rangle)$ .
2. Double excitation: When  $i \neq h$ , we set  ${}^1|\Phi_{ih}^{ll}\rangle = \frac{1}{\sqrt{2}}(|\Phi_{ih}^{ll}\rangle + |\Phi_{\bar{i}\bar{h}}^{\bar{l}\bar{l}}\rangle)$ . When  $i = h$ , we set  ${}^1|\Phi_{ih}^{ll}\rangle = |\Phi_{hh}^{ll}\rangle$ . When  $j \neq h, b \neq l$ , we set  $|D_{hj}^{lb}\rangle_A = (|\Phi_{hj}^{lb}\rangle + |\Phi_{\bar{h}\bar{j}}^{\bar{l}\bar{b}}\rangle) / 2$  and  $|D_{hj}^{lb}\rangle_B = [2(|\Phi_{hj}^{lb}\rangle + |\Phi_{\bar{h}\bar{j}}^{\bar{l}\bar{b}}\rangle) + (|\Phi_{hj}^{ll}\rangle + |\Phi_{\bar{h}\bar{j}}^{\bar{l}\bar{l}}\rangle) - (|\Phi_{jh}^{lb}\rangle + |\Phi_{\bar{j}\bar{h}}^{\bar{l}\bar{b}}\rangle)] / \sqrt{12}$ .
3. Triple excitation:  $|T_{hh\bar{i}}^{lla}\rangle = (|\Phi_{hh\bar{i}}^{lla}\rangle + |\Phi_{hh\bar{i}}^{\bar{l}\bar{l}\bar{a}}\rangle) / \sqrt{2}$ .

### III. RESULTS

Below, we will report results for the electronic structure methods presented above according to the following parameter settings: the impurity on-site coulomb repulsion is set to  $U = 0.1$ , the hybridization width is set to  $\Gamma = 0.01$ , the energy spacing for the bath states is set to  $\Delta E = 0.001$  (i.e., the density of the bath states is set to  $\rho(\epsilon) = 1000$ ), the relative energy difference between two impurity sites is set to  $\Delta\epsilon = 0$  and the hopping strength between two impurity sites is set to  $t_d = 0.2$ .

**III.A. Impurity Population  $n_1(\epsilon_d)$  and  $n_2(\epsilon_d)$ .** We begin by analyzing population results for the impurity in the electronic ground state  $|\Psi_0\rangle$ ,  $\langle n_{1\uparrow}\rangle \equiv \langle \Psi_0 | \hat{d}_{1\uparrow}^\dagger \hat{d}_{1\uparrow} | \Psi_0 \rangle$ , according to the different selective CI methods in Table 1. As a test of each method, we set  $\Delta\epsilon_d = 0$ , and in Figure 3, we report  $\langle n_{1\uparrow}\rangle$  as a function of  $\epsilon_d$ , the energy of the  $d_1$  and  $d_2$  impurities. Since both impurities are given the same energy, we find that their populations are almost identical (not shown). As a practical matter, in Figure 3, we find three different plateau regimes:

- In the range  $\epsilon_d < -0.3$ ,  $n(\epsilon_d) = 4$ , there are four electrons in total on the impurities and  $d_{1\uparrow}$ ,  $d_{1\downarrow}$ ,  $d_{2\uparrow}$ , and  $d_{2\downarrow}$  are all occupied.
- In the range  $-0.3 < \epsilon_d < -0.26$ ,  $n(\epsilon_d) = 3$ , there are three electrons in total on the impurities.
- In the range  $-0.26 < \epsilon_d < +0.15$  (not shown completely),  $n(\epsilon_d) = 2$ , there are two electrons in total on the impurities.

Although Figure 3 is limited to the region  $\epsilon_d < -0.24$ , two more plateaus can be identified (not shown):

- In the range  $0.15 < \epsilon_d < 0.19$ ,  $n(\epsilon_d) = 1$ , there is one electron in total on the impurities.
- In the range  $\epsilon_d > 0.19$ ,  $n(\epsilon_d) = 0$ , there is no electron on the impurities.

Altogether, by changing  $\epsilon_d$ , we can isolate four different electron transfer (ET) processes. The first ET process happens around  $\epsilon_d = -0.3$  and the second ET process happens around  $\epsilon_d = -0.26$ .

Now, when analyzing Figure 3a, the first thing one notices is that MFT (incorrectly) does not predict a plateau over the regime  $-0.29 < \epsilon_d < -0.26$ , where  $n(\epsilon_d) \approx 3$ . Given this failure,

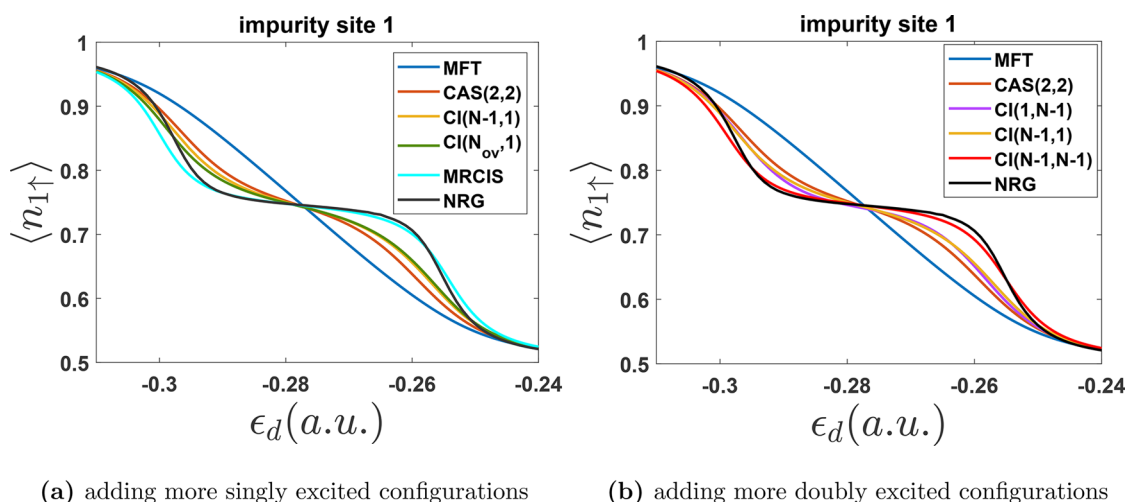
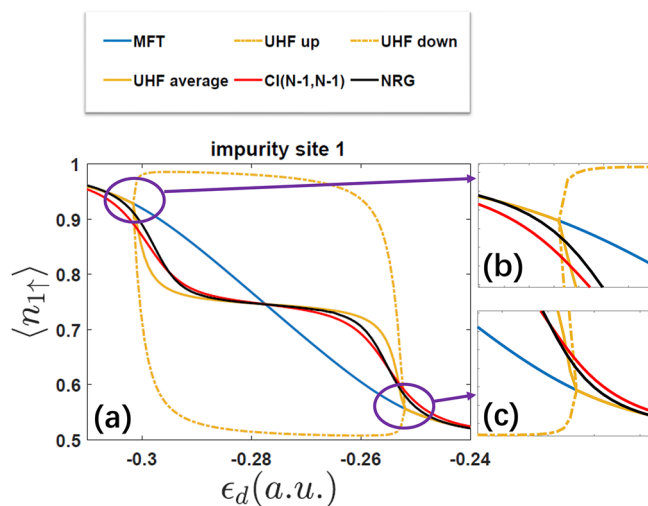


Figure 3. Impurity population results from different choices of configurations for  $t_d = 0.2$  and  $\Delta\epsilon_d = 0$ . (a) We include more singly excited configurations, and (b) we include more doubly excited configurations. Note that adding more doubly excited configurations is more effective at recovering the plateau around  $\epsilon_d = -0.29$  and  $\epsilon_d = -0.26$  than is adding more singly excited configurations.

in Figure 3a, we consider the effect of adding in more singly excited configurations, analyzing (in order) CAS(2,2), CI(N-1,1) and CI(N<sub>ov</sub>,1). These three methods differ in terms of the number of singly excited configurations, but they all include exactly one doubly excited configuration  $|\Phi_{hh}^{ll}\rangle$ . We find that, compared to the MFT results, CAS(2,2) gives a huge correction; however, adding more singly excited configurations does not yield results that are significantly closer to the exact NRG results. Note that, while MRCIS results [on top of a set of three CAS(2,2) reference states] do agree reasonably well with exact NRG calculations, MRCIS includes both singles and doubles. (Overall, as a side note, the data shows that running a large MRCIS calculation is likely not worth the trouble; the results are not much better than a CI(N-1, N-1) calculations, whereas the cost is at least 2 orders of magnitude more.)

Next, in Figure 3b, we consider the effect of adding in more doubly excited configurations, analyzing (in order) { CAS(2,2), CI(N-1,1) } versus { CI(1,N-1), CI(N-1,N-1) }. The former set includes only one doubly excited configuration  $|\Phi_{hh}^{ll}\rangle$  whereas the latter set includes N-1 doubly excited configurations of the form  $\{^1|\Phi_{hh}^{ll}\rangle, ^1|\Phi_{hh}^{al}\rangle\}$ . Within each of these sets, we include a different number of singly excited configurations, either just  $\{|S_h^l\rangle\}$  or  $\{|S_h^l\rangle, |S_h^a\rangle\}$ . Among all of these different selective CI methods, only CI(N-1,N-1) nearly matches the NRG results, and luckily with a relatively small number of configurations.

At this point, having analyzed quite a few restricted CI approaches, in Figure 4, we compare the most promising restricted CI method [CI(N-1,N-1)] against the simplest unrestricted method, unrestricted Hartree-Fock (UHF). For UHF, one breaks symmetry such that  $\langle n_{1\uparrow} \rangle \neq \langle n_{1\downarrow} \rangle$ . For this reason, in order to compare UHF results vs NRG results, we will need to average the two solutions:



**Figure 4.** Electron population on impurity site 1 for  $t_d = 0.2$  and  $\Delta\epsilon_d = 0$ . (a) Range is  $-0.31 < \epsilon_d < -0.24$ , where the total number of electrons on impurities  $n(\epsilon_d)$  satisfies:  $4 \geq n(\epsilon_d) \geq 2$ ; (b, c) Zoom in on the two UHF discontinuity regions. We plot MFT (mean-field), UHF up/down (unrestricted Hartree-Fock for spin up/down electron), UHF average (averaged results of UHF up and down), CI(N-1,N-1) and NRG (numerical renormalization group theory). The NRG results are effectively exact. Note that MFT is smooth but inaccurate, whereas UHF is accurate in the plateau region but discontinuous around  $\epsilon_d = -0.3$  and  $\epsilon_d = -0.25$ .

$$\bar{n}_1 = \frac{\langle n_{1\uparrow} \rangle + \langle n_{1\downarrow} \rangle}{2} \quad (18)$$

From Figure 4, one can clearly see that the UHF average in eq 18 reproduces the plateau region where  $n(\epsilon_d) = 3$  very well. Nevertheless, as the insets in parts b and c of Figure 4 show clearly, the UHF ansatz introduces an artificial discontinuity at the edge points of the plateau region ( $\epsilon_d \approx -0.3$  or  $\epsilon_d \approx -0.25$ ) where there is a Coulson-Fisher point<sup>77</sup> and the solution switches between restricted and unrestricted wave functions (and electron transfer occurs). At these points,  $\frac{\partial n(\epsilon_d)}{\partial \epsilon_d}$  is clearly discontinuous. Although such discontinuities can be addressed by invoking a broken-symmetry (BS) UHF solution (see the Supporting Information), given our long-term interests in dynamics and need for smooth ground and excited states, we will not focus too much here on UHF solutions (though see also Section IV.A.1).

**III.B. Total Energy.** Beyond impurity populations, if one wants to either calculate thermodynamic quantities or simulate dynamical trajectories, the most important quantity of interest is the total energy of the universe (molecule + metal). To best understand the merits of the CI approaches described above, in Figure 5, we plot the first three state energies (or Hamiltonian eigenvalues) as calculated by<sup>78</sup>

- CI(N-1,N-1), the method which performed best above at recovering impurity populations.
- CI(N<sub>ov</sub>,1), the CI method with the largest number of configurations; see Table 1

In Figure 5, we find that in the energy regime  $-0.3 < \epsilon_d < -0.26$ , where  $n(\epsilon_d) = 3$ , including doubly excited configurations is crucial as far as minimizing the ground state energy. And including doubly excited configurations is more important than including singly excited configurations, which seemingly agrees with the Brillouin's theorem ( $\langle \Psi_{HF} | S_i^a \rangle = 0$ ). This finding helps explain why the CI(N-1,N-1) method performed so well at recovering  $\langle n_{1\uparrow} \rangle = \langle \Psi_0 | d_{1\uparrow}^\dagger d_{1\uparrow} | \Psi_0 \rangle$  in Figure 4. However, note that (in fairness), Figure 5 also makes clear that, when calculating excited states (especially in the  $n(\epsilon_d) = 4$  and  $n(\epsilon_d) = 2$  regions), CI(N<sub>ov</sub>,1) finds significantly lower variational energies.<sup>79,80</sup>

Finally, having convinced ourselves of the importance of adding in doubly excited configurations, it is instructive to compare the energies of the final CI(N-1,N-1) eigenvalues with the set of essential CAS(2,2) configurations,  $\{|\Phi_{HF}\rangle, |S_h^l\rangle, |\Phi_{hh}^{ll}\rangle\}$ ; such a comparison will hopefully yield simple insight as to if/when a sophisticated CI approach is needed. In Figure 6a, we plot the energies of these essential configurations, as well as the three lowest energies found after the CI(N-1,N-1) diagonalization. We find that, when the energy of the doubly excited configuration  $|\Phi_{hh}^{ll}\rangle$  approaches the energy of the HF state  $|\Phi_{HF}\rangle$  (and nearly crosses the energy of the singly excited configuration  $|S_h^l\rangle$ ), there is a huge correction to the ground state energy. This avoided crossing occurs in the regime  $\epsilon_d \approx -0.28$ ,  $n(\epsilon_d) \approx 3$ ; see Figure 6b.

As a side note, the reader can also discern from Figure 6 that, even for a modest CI calculation (e.g., CI(N-1,N-1)), the predicted first excited state energy,  $E_1$  CI(N-1,N-1), is far away from the energy of the HOMO-LUMO transition,  $E_h^l$ . Thus, as mentioned above, one must be careful in how one assesses the value of excited state calculations for a large CI calculation with a continuum of states; in this instance, excited states need to be

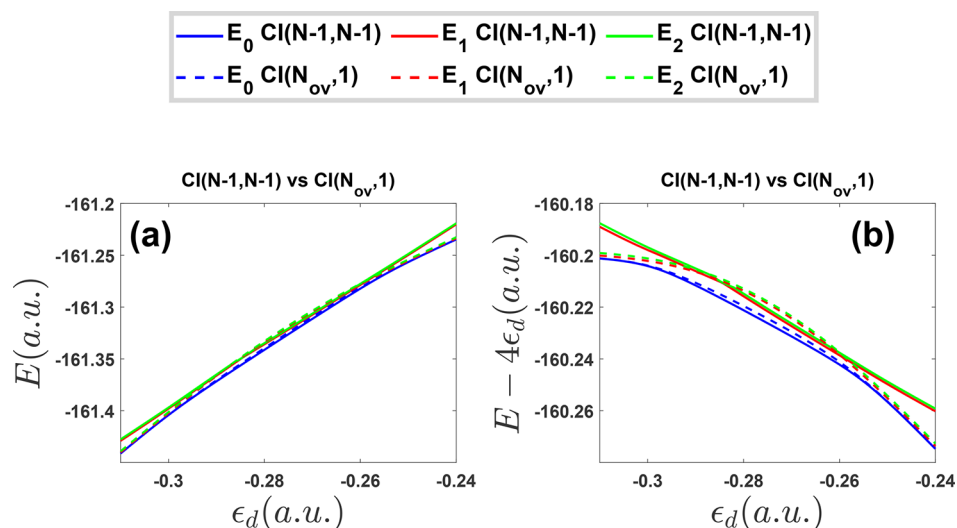


**Figure 5.** CI(N-1,N-1) (solid line) and CI(N<sub>ov</sub>,1) (dashed line) results for the lowest three state energies (eigenvalues) for  $t_d = 0.2$  and  $\Delta\epsilon_d = 0$ . Within the range  $-0.31 < \epsilon_d < -0.24$ , the total number of electrons on the impurities is between 4 and 2 ( $2 \leq n(\epsilon_d) \leq 4$ ). (a) Total energy  $E$  versus  $\epsilon_d$ . (b)  $E - 4\epsilon_d$  versus  $\epsilon_d$ . The subplot (b) is included in order to compare CI(N-1,N-1) results versus CI(N<sub>ov</sub>,1) results more clearly near the crossing point. Note that in Figure 5b, CI(N-1,N-1) finds the lower ground state and excited states energies when  $-0.3 < \epsilon_d < -0.26$ .

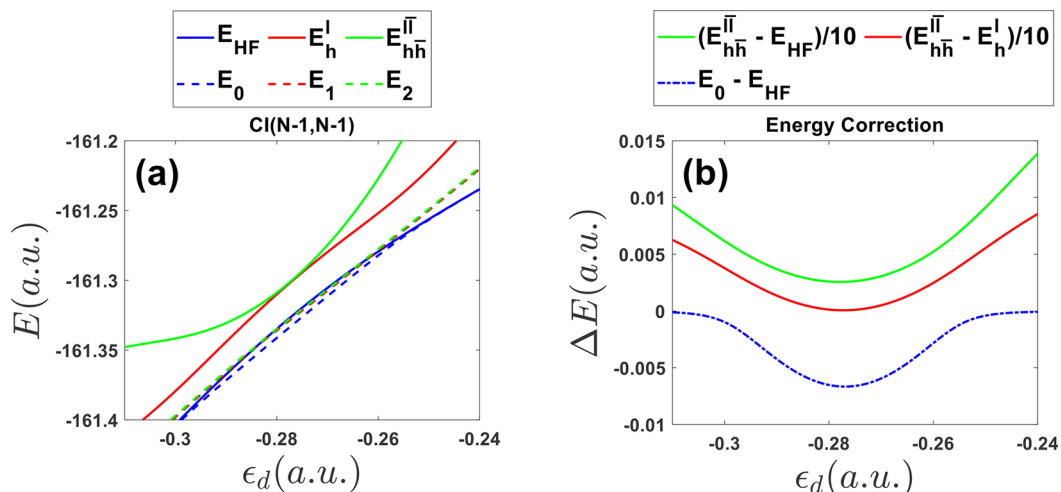


**Figure 6.** (a) Three lowest raw configuration energies (solid line). These are labeled as  $E_{HF}$ ,  $E_h^I$  and  $E_{hh}^{II}$ , corresponding to the energies of the Hartree–Fock ground state configuration, the HOMO-to-LUMO singly excited configuration and the HOMO-to-LUMO doubly excited configuration, respectively. The three lowest CI(N-1,N-1) eigenvalues (dashed line) are labeled as  $E_0$ ,  $E_1$ , and  $E_2$ . (b) Relationship between the ground state energy correction (blue dash-dotted line) and the energy differences between configurations (red and green solid line). Part b demonstrates that the absolute value of the ground state energy correction is a maximum when the energy of the HOMO-to-LUMO doubly excited configuration is closest both to the energy of the HF ground state configuration and to the energy of the HOMO-to-LUMO singly excited configuration. Note that, with parameter settings  $t_d = 0.2$  and  $\Delta\epsilon_d = 0$ , the maximum CI(N-1,N-1) correction to the ground state can be as large as 0.005 hartree.

understood as part of a dense set of states and the accuracy of these states can only be determined dynamically.

## IV. DISCUSSION

**IV.A. Electron Transfer from an Open Shell Impurity Singlet to the Metal.** The results presented above should convince the reader that, at least for a model Hamiltonian with two impurity sites, one can recover reasonable results using basic configuration interaction theory. Now, one might be tempted to think that having two impurity sites is not so different from having one (dressed) impurity site.<sup>81</sup> Unfortunately, the latter statement is incorrect. After all, in a certain parameter regime, one should find dynamics characterized by the Figure 7.

In other words, one can imagine electron transfer from an *open shell singlet* residing on the impurity (with two sites!) to the

metal. Such rich physics cannot be captured by a one-site impurity model. And yet, capturing such physics would clearly be essential for modeling how a chemical bond breaks on a metal surface.

**IV.A.1. Vary  $t_d$  (Keeping  $\Delta\epsilon_d = 0$ ).** To better understand the nature of electron transfer from an *open shell singlet* on an impurity into a metal substrate, we have rerun all the calculations presented above with different parameters for  $t_d$ . After all, when  $t_d$  is large, we can expect large hybridization of the impurity orbitals (and therefore, if the number of electrons is even, the impurity should prefer to be in a closed shell singlet). However, if  $t_d$  is small and the number of electrons is even, we can expect the impurity will prefer an *open shell singlet* configuration (as in Figure 7). This is the same as a Mott transition.<sup>82</sup>

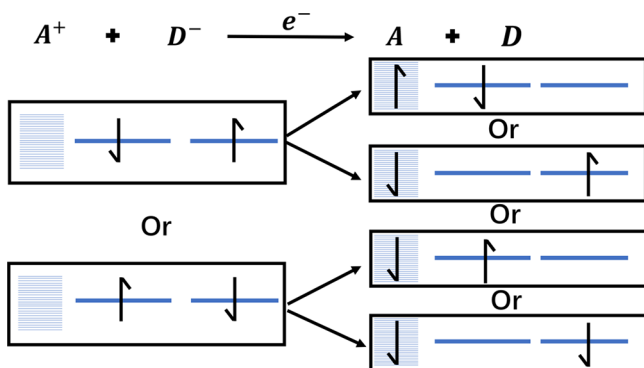


**Figure 7.** Schematic figure for an open-shell impurity singlet electron transfer. Note that when  $t_d$  is small, the electronic state of the impurity tends to have more of an open shell character.

In Figure 8b, we benchmark  $\text{CI}(N-1, N-1)$  for several different values of  $t_d$ , ranging from  $t_d = 0.2$  to  $t_d = 0.02$ . For large values of  $t_d$  ( $t_d > 0.1$ ), we find that indeed,  $\text{CI}(N-1, N-1)$  results do match the exact NRG results. However, for small values of  $t_d$  ( $t_d < 0.1$ ),  $\text{CI}(N-1, N-1)$  fails. In Figure 8b, we find an anomalously large (and incorrect) plateau when  $t_d = 0.02$ .

In order to address this failure, one can argue that it is appropriate to include one more doubly excited configuration. The reason is as follows. Consider the case when  $\langle n \rangle / 2 = \langle n_1 \rangle = \langle n_2 \rangle = 1.5$  ( $\langle n_2 \rangle$  not shown in the figure) in Figure 8b. For this value of  $\epsilon_d$ , if we diagonalize the mean-field impurity Hamiltonian  $\hat{H}_{\text{imp}}$

$$\hat{H}_{\text{imp}} = \begin{pmatrix} \epsilon_d + U\langle n_2 \rangle & t_d \\ t_d & \epsilon_d + U\langle n_1 \rangle \end{pmatrix} \quad (19)$$

we recover two orbital energies (two eigenvalues):

$$\begin{aligned} \epsilon_{h-1} &= \epsilon_d + U\langle n \rangle / 2 - t_d \\ \epsilon_h &= \epsilon_d + U\langle n \rangle / 2 + t_d \end{aligned} \quad (20)$$

Thereafter we must place 3 electrons into these two orbitals since  $\langle n \rangle = 3$ . Now, because of electron–electron repulsion, one can expect that a lower energy ground state can be found by unrestricting the calculation, leading to a new set of energies for which the  $\alpha$  orbitals are shifted in energy from the  $\beta$  orbitals (by an amount that we call  $U_{\text{eff}}$ ). In such a case, the HOMO and

HOMO–1 orbitals will be different for  $\alpha$  and  $\beta$  spin (without loss of generality, we assume  $\epsilon_i < \epsilon_j$ ):

$$\begin{aligned} \epsilon_{h-1} &= \epsilon_d + U\langle n \rangle / 2 - t_d \\ \epsilon_{h-1}^{\bar{}} &= \epsilon_d + U\langle n \rangle / 2 - t_d + U_{\text{eff}} \\ \epsilon_h &= \epsilon_d + U\langle n \rangle / 2 + t_d \\ \epsilon_h^{\bar{}} &= \epsilon_d + U\langle n \rangle / 2 + t_d + U_{\text{eff}} \end{aligned} \quad (21)$$

Now if  $t_d$  is large in the sense that  $2t_d > U_{\text{eff}}$  (for our results,  $t_d = 0.2$ ,  $U = 0.1$ , so we assume  $U_{\text{eff}}$  is smaller than 0.1), the energy ordering of the orbitals is standard:  $\epsilon_{h-1} < \epsilon_{h-1}^{\bar{}} < \epsilon_h < \epsilon_h^{\bar{}}$ . However, if  $t_d$  is small in the sense that  $2t_d < U_{\text{eff}}$  (e.g.,  $t_d = 0.02$ ), the energy ordering of the orbitals inverts:  $\epsilon_{h-1} < \epsilon_h < \epsilon_{h-1}^{\bar{}} < \epsilon_h^{\bar{}}$ . Thus, in the small  $t_d$  limit, if we consider the case when two electrons are excited from occupied orbitals to virtual orbitals, the doubly excited configurations  $|\Phi_{h-1h-1}^{\bar{}}\rangle$  as well as  $|\Phi_{hh}^{t_d t_d}\rangle$  should play an important role in a CI calculation. For this reason, we have included one more CI method in Table 1, namely  $\text{CI}(N-1, N+1)$ , for which we include two extra configurations,  $|\Phi_{h-1h-1}^{\bar{}}\rangle$  and  $|\Phi_{hh}^{t_d t_d}\rangle$ . In Figure 8a, we demonstrate that  $\text{CI}(N-1, N+1)$  does recover the correct populations quantitatively.

Now, the argument above may appear cyclical and flawed. After all, the interpretation above was entirely predicated on the idea that, for small  $t_d$ , one would find an *open shell singlet* on the impurity—and yet we never actually proved as much. To verify that, indeed, an *open shell singlet* appears, in Figures 9 and 10, we analyze (in detail) the electronic structure of the impurity sites across the whole  $\epsilon_d$  range for the different  $t_d$  values, one large ( $t_d = 0.2$ ) and one small ( $t_d = 0.02$ ). In Figures 9 and 10, we plot single occupancy results (a, b) ( $\langle n_{1\uparrow} \rangle$  and  $\langle n_{2\uparrow} \rangle$ ), double occupancy results (c, d) and the correlation between single and double occupancy (e, f). We plot results for  $\text{CI}(N-1, N-1)$ ,  $\text{CI}(N-1, N+1)$  and UHF (and all relative to exact NRG calculations).

For  $t_d = 0.2$ , in Figure 9, we find that, as far as the total number of electrons present (in Figure 9a–d), the  $\text{CI}(N-1, N-1)$  and  $\text{CI}(N-1, N+1)$  results are nearly identical, and they nearly agree with the exact NRG results (as does UHF). Now if one looks closely in the regions  $\epsilon_d \in [-0.25, -0.24]$  and  $\epsilon_d \in [0.14, 0.15]$ , there are small differences. Indeed, in these two  $\epsilon_d$  regions, where the total number of electrons in the molecule is changing from 3 to 2 and from 2 to 1, respectively, the plot of correlation

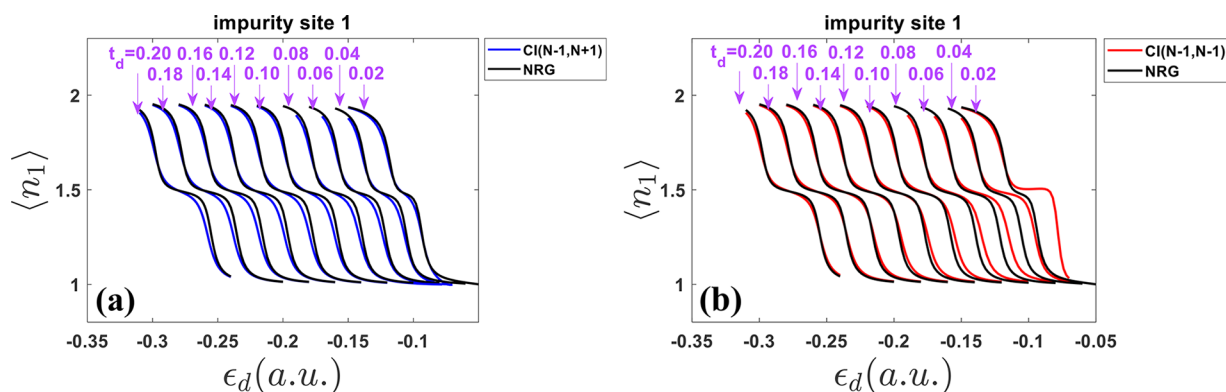


**Figure 8.**  $\text{CI}(N-1, N+1)$  (blue solid line in part a),  $\text{CI}(N-1, N-1)$  (red solid line in part b) and NRG (black solid line) results for impurity population as a function of impurity energy  $\epsilon_d$  for different  $t_d$  with  $\Delta\epsilon_d = 0$ . The hopping strength between two impurity sites  $t_d$  ranges from 0.02 to 0.2. Note that  $\text{CI}(N-1, N-1)$  fails for small  $t_d$  while  $\text{CI}(N-1, N+1)$  results match the NRG results for all values of  $t_d$ .

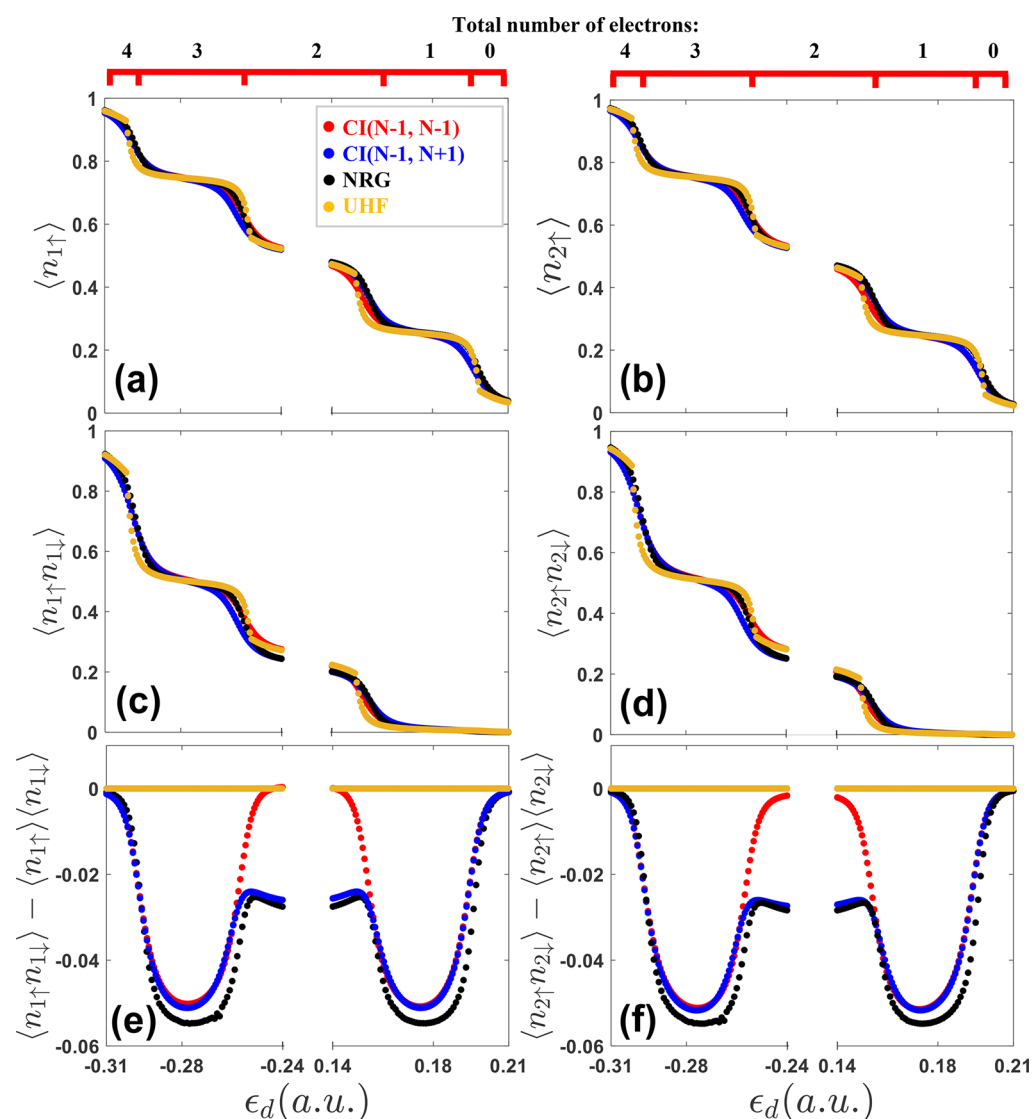


**Figure 9.** Single occupancy, double occupancy, and occupancy correlation on each impurity site for  $t_d = 0.2$  and  $\Delta\epsilon_d = 0$ . (a) Single occupancy on impurity site 1. (b) Single occupancy on impurity site 2. (c) Double occupancy on impurity site 1. (d) Double occupancy on impurity site 2. (e) Correlation on impurity site 1 ( $\langle n_{1\uparrow}n_{1\downarrow} \rangle - \langle n_{1\uparrow} \rangle \langle n_{1\downarrow} \rangle$ ). (f) Correlation on impurity site 2 ( $\langle n_{2\uparrow}n_{2\downarrow} \rangle - \langle n_{2\uparrow} \rangle \langle n_{2\downarrow} \rangle$ ). Note that CI(N-1,N-1) performs well as compared with NRG. However, also note that there is not very much electron–electron correlation in parts e and f (the maximum is only 0.06).

(in Figure 9e,f) makes clear that CI(N-1,N+1) and CI(N-1,N-1) are not identical; and over the entire region where  $n(\epsilon_d) = 2$ , i.e.,  $\epsilon_d \in [-0.24, 0.14]$ , CI(N-1,N+1) agrees with NRG (whereas CI(N-1,N-1) does not). Nevertheless, one should note that the scale on parts e and f of Figure 9 is not very large (as compared with parts e and f of Figure 10). One should also note that, in this figure, the correlation between single and double occupancy is not maximized in the central  $n(\epsilon_d) = 2$  region (where  $\epsilon_d \in [-0.24, 0.14]$ ), but rather in the outer  $n(\epsilon_d) = 3$  ( $\epsilon_d = -0.28$ ) and  $n(\epsilon_d) = 1$  ( $\epsilon_d = 0.18$ ) regions. Altogether, this data suggests that electron correlation exists (but is not very strong) for  $t_d = 0.2$ , which explains why CI(N-1,N-1) performs so well in Figure 9a–d.

Next, let us turn to Figure 10, where we plot results for the case  $t_d = 0.02$ . Here, we immediately see enormous differences between CI(N-1,N-1) and the exact NRG results both in terms of the single and double occupancy results. At certain values of  $\epsilon_d$ , UHF can nearly match the NRG results, but not always, especially in the regions of electron transfer (where clear discontinuities arise at each step of the curve). By contrast to the

other methods, the CI(N-1,N+1) results match the NRG results quite well at almost all points. One can draw the same conclusions from parts e and f of Figures 10 with regard to electron correlation. Finally, note that, in contrast to the case  $t_d = 0.2$ , here we find the strongest correlation effects within the middle range for  $\epsilon_d$  ( $\epsilon_d \approx -0.05$ ,  $n(\epsilon_d) \approx 2$ ), confirming our premise that an *open shell singlet* is prominent for the case of small  $t_d$ . Note also that the correlation strength is about three times as big for the  $t_d = 0.02$  case as for the  $t_d = 0.2$  case. Overall, the conclusions from this data are that, if we include just two extra doubly excited configurations, we can really recover the lion’s share of electron correlation for a two-site impurity model on a metal surface.

**IV.A.2. Vary  $\Delta\epsilon_d$  (keeping  $t_d = 0.2$ ).** So far, within this manuscript, we have always insisted that the two sites have the same energy ( $\epsilon_{d1} = \epsilon_{d2} = \epsilon_d$ ). At this point, we will break this assumption as another means of testing the quality of the CI approaches above. Let  $\Delta\epsilon_d \equiv \epsilon_{d2} - \epsilon_{d1}$ . In Figure 11, for different  $\Delta\epsilon_d$  (ranging from  $\Delta\epsilon_d/t_d = -1$  to  $\Delta\epsilon_d/t_d = 1$ ), we plot population results as a function of  $\epsilon_d$  over a range so that the total

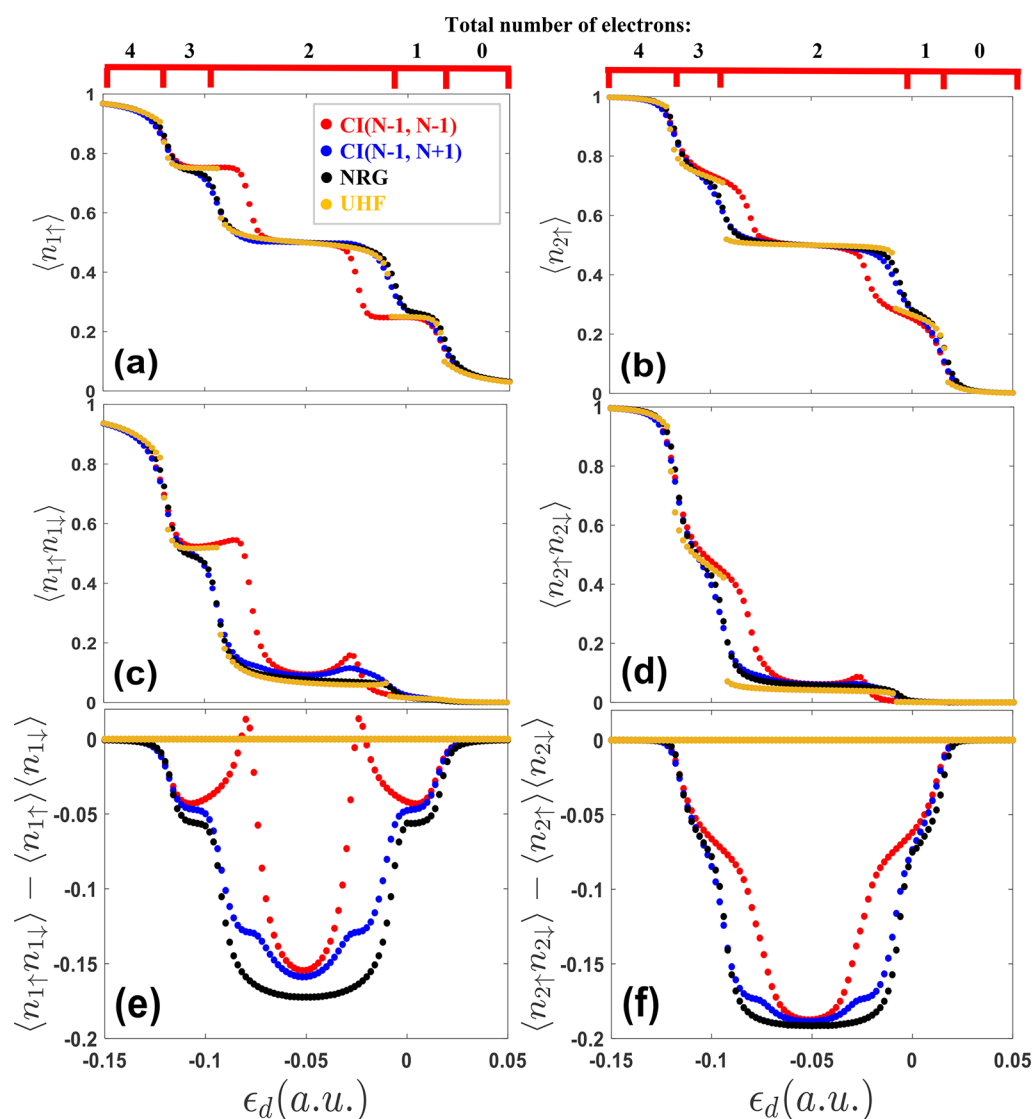


**Figure 10.** Single occupancy, double occupancy, and occupancy correlation on each impurity site for  $t_d = 0.02$  and  $\Delta\epsilon_d = 0$ . (a) Single occupancy on impurity site 1. (b) Single occupancy on impurity site 2. (c) Double occupancy on impurity site 1. (d) Double occupancy on impurity site 2. (e) Correlation on impurity site 1 ( $\langle n_{1\uparrow}n_{1\downarrow} \rangle - \langle n_{1\uparrow} \rangle \langle n_{1\downarrow} \rangle$ ). (f) Correlation on impurity site 2 ( $\langle n_{2\uparrow}n_{2\downarrow} \rangle - \langle n_{2\uparrow} \rangle \langle n_{2\downarrow} \rangle$ ). Note that in parts e and f, the depth of the correlation single well is about 0.2, which is three times bigger than that for  $t_d = 0.2$  case (which was plotted in Figure 9). For this data set, CI(N-1, N+1) vastly outperforms CI(N-1, N-1).

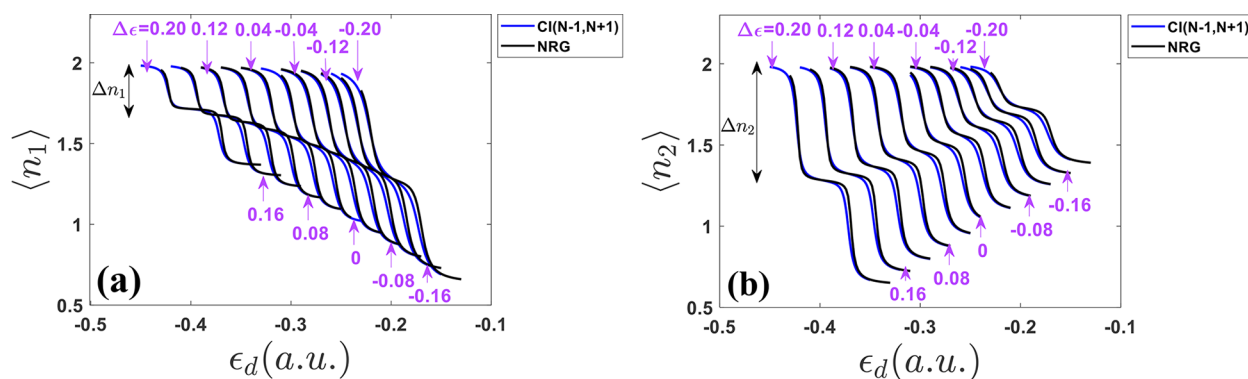


**Figure 11.** CI(N-1, N+1) (blue solid line) and NRG (black solid line) results for impurity population on (a) the impurity site 1 and (b) the impurity site 2 as a function of impurity energy  $\epsilon_d$  for different  $\Delta\epsilon_d$  with  $t_d = 0.2$ . Here we define:  $\Delta\epsilon_d \equiv \epsilon_{d2} - \epsilon_{d1}$ . The relative energy difference between two impurity sites  $\Delta\epsilon_d$  ranges from  $-0.2$  to  $+0.2$ .  $\Delta n_1$  and  $\Delta n_2$  represent the longitudinal distance of the first plateau and the second plateau for the impurity site 1 and the impurity site 2, respectively. Note that CI(N-1, N+1) results match the NRG results for all different  $\Delta\epsilon_d$ .

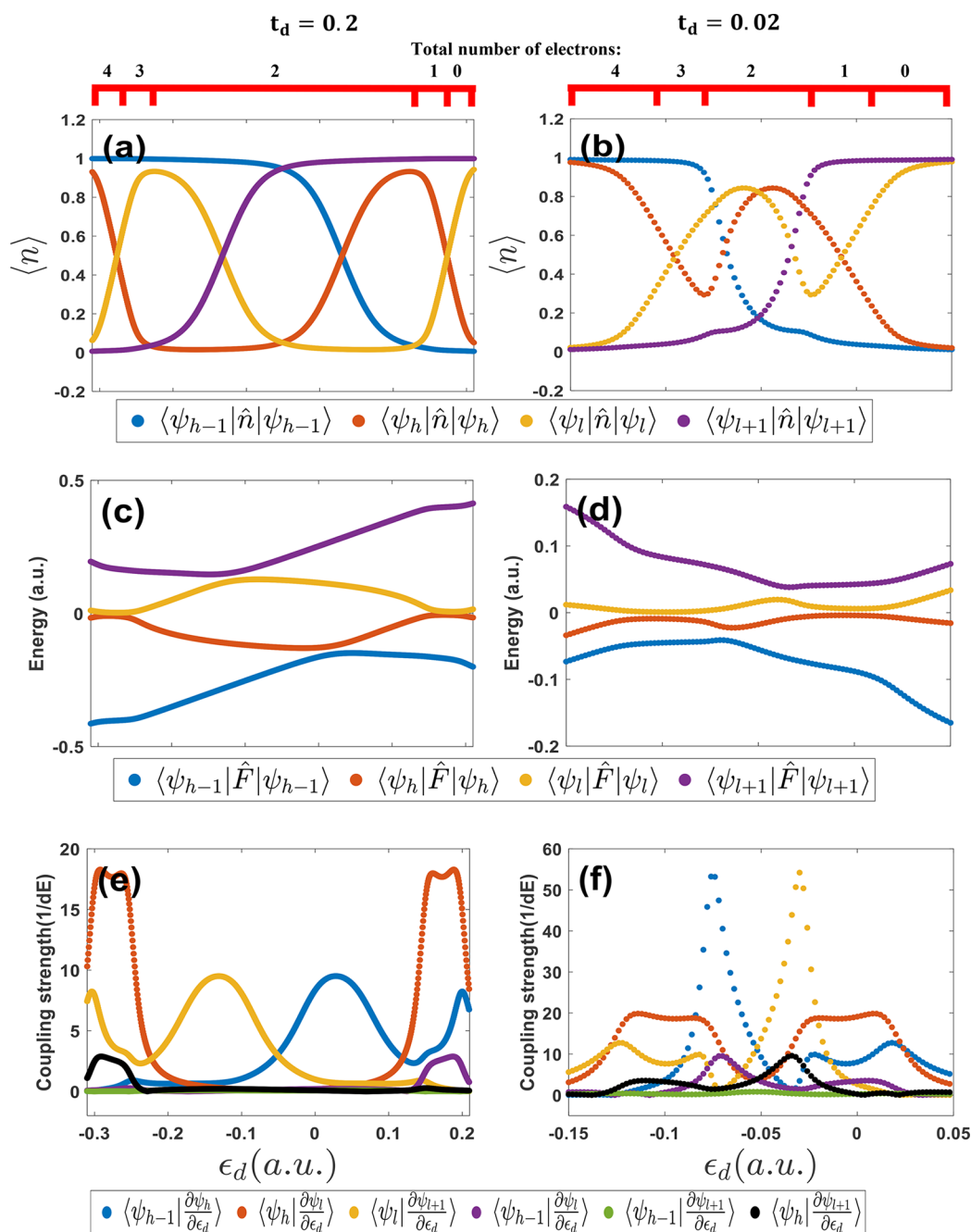


**Figure 12.** (a, b) Impurity population for the occupied entangled orbitals (OEOs) and virtual entangled orbitals (VEOs) for (a)  $t_d = 0.2$  and (b)  $t_d = 0.02$ . (c, d) Orbital energies of OEOs and VEOs for (c)  $t_d = 0.2$  and (d)  $t_d = 0.02$ . (e, f) Derivative couplings between OEOs and VEOs (e)  $t_d = 0.2$  and (f)  $t_d = 0.02$ . Note that HOMO-1/LUMO+1 mixing remains zero for all  $\epsilon_d$  so we do not include the configuration  $|\Phi_{h-1, h-1}^{l+1, l+1}\rangle$  into the calculation.

number of electrons on the two impurities changes from 4 to 3 to 2. Our focus here will be on the first electron transfer process (i.e., the drop between the first two plateaus farthest on the left). Here, we see that when one electron is transferred from the molecule to the metal, this transfer occurs at different values of  $\epsilon_d$  (depending on  $\Delta\epsilon_d$ ). If we define  $\Delta n_1$ ,  $\Delta n_2$  to be the number of electrons extracted from impurity site 1 and site 2 (respectively) at the first plateau, we must obviously have  $\Delta n_1 + \Delta n_2 = 1$ . As we can see from Figure 11, when  $\Delta\epsilon_d$  decreases,  $\Delta n_1$  increases and  $\Delta n_2$  decreases. In other words, the impurity site with a higher ionization energy will lose more electronic density during the first electron transfer process.

Three simple limits can be identified here:

1. When  $\Delta\epsilon_d = 0$ ,  $\Delta n_1 = \Delta n_2 = 0.5$ .
2. When  $\Delta\epsilon_d \gg |t_d|$ ,  $\Delta n_1 \rightarrow 0$ ,  $\Delta n_2 \rightarrow 1$ .
3. When  $\Delta\epsilon_d \ll -|t_d|$ ,  $\Delta n_1 \rightarrow 1$ ,  $\Delta n_2 \rightarrow 0$ .

Note that there is an asymmetry to the electron transfer process described above. In our model, only impurity site 1 is coupled directly to the metal so that, if the energy levels of site 1 and site 2 are not resonant, site 2 is coupled to the metal only indirectly and that indirect hybridization coupling (i.e., a superexchange matrix element) will be very small. Thus, within scenario 2 above, when the energy of impurity site 2 is far higher in energy than site 1 (so that the first electron will be extracted from site 2 and not site 1), the change in the impurity population on site 2 as a function of  $\epsilon_d$  will look like a step function. See

Figure 11b. Nevertheless, in all cases, we note that  $CI(N-1, N+1)$  remains very accurate.

**IV.B. A Picture of Electron Transfer in Terms of Orbitals.** Above, we have shown that, for the case  $t_d = 0.2$ ,  $CI(N-1, N-1)$  is applicable and can offer a reasonably accurate level of theory in terms of impurity population; however, for the case  $t_d = 0.02$ ,  $CI(N-1, N+1)$  is necessary. At this point, it is worthwhile to explain the difference between these two cases, and why two extra configurations can be so important. To do so, we will focus on the behavior of the relevant orbitals (two occupied entangled orbitals (OEOs)  $\{|\psi_{h-1}\rangle, |\psi_h\rangle\}$  and two virtual entangled orbitals (VEOs)  $\{|\psi_l\rangle, |\psi_{l+1}\rangle\}$ ). (For a discussion of the behavior of the relevant configurations, see the S.I.)

In Figure 12, we plot the impurity populations (a, b) and energies (c, d) of the entangled orbitals; in parts (e, f), we plot the derivative couplings between the entangled orbitals, which highlights how these orbitals change as a function of energy  $\varepsilon_d$  (or really as a function of some abstract nuclear coordinate).

We begin with the  $t_d = 0.2$  case and we focus on how electrons move from the impurity to the bath in the region  $\varepsilon_d \in [-0.31, -0.24]$ . In this region, according to Figure 12c, there is a crossing between the HOMO and the LUMO; and according to Figure 12a, one can ascertain that one of these orbitals is localized on the impurity, one is delocalized in the bath, so that their crossing carries the information about charge transfer (when the impurity moves from a charge state of  $-4$  to  $-2$ ). For this reason, one would predict that the adiabatic ground state should be composed of primarily  $\{|\Phi_{HF}\rangle, |S_h^l\rangle, |\Phi_{hh}^{\parallel}\rangle\}$  and a CAS (2,2) calculation should be able to offer a meaningful correction to the HF solution.

Notice, however, that the HOMO-1 and the LUMO+1 orbitals do not cross with any other orbitals in this energy window: one can see that the HOMO-1 crosses with the HOMO at  $\varepsilon_d = 0.02$  (and the LUMO+1 crosses with the LUMO at  $\varepsilon_d = -0.1$ ), and these  $\varepsilon_d$  values are well within the plateau region where the impurity has a relatively constant charge of  $-2$ . Quantitatively, from Figure 12e, we notice that the derivative couplings between the LUMO and the LUMO+1 is centered at  $\varepsilon_d = -0.1$  and is well separated from the center of the derivative couplings between the HOMO and the LUMO (which is centered at  $\varepsilon_d = -0.25$ ). Apparently, for this value of  $t_d$ , the HOMO-1 and the LUMO+1 do not play a very large role in modulating the charge transfer between the HOMO and the LUMO and predicting impurity populations. Nevertheless, the mixing of HOMO-1/HOMO and LUMO+1/LUMO does explain why the configurations  $\{|\Phi_{hh}^{l+1}\rangle, |\Phi_{hh-1}^{\parallel}\rangle\}$  are necessary to describe electron-electron correlation *quantitatively*, as shown in parts (e) and (f) of Figure 9.

Next, we turn to the case  $t_d = 0.02$ . For this case, the impurity changes charge from  $-4$  to  $-2$  over the region  $\varepsilon_d \in [-0.15, -0.08]$ . Within this range, according to parts b and d of Figure 12, we now find two crossings: one crossing between the HOMO and the LUMO (similar the case of  $t_d = 0.2$ ) and another crossing between the HOMO-1 and the HOMO (which is not similar the case of  $t_d = 0.2$ ). Moreover, unlike the  $t_d = 0.2$  case, the HOMO-1 is not always localized to the impurity. Thus, both the HOMO and the HOMO-1 will contribute to the total two-electron transfer (one electron transferred in each step). This point is made even clearer when we look at the derivative couplings in Figure 12f. Here, we find that the derivative coupling between the HOMO and the HOMO-1 overlaps with the derivative coupling between the

HOMO and the LUMO, highlighting the fact that one cannot fully isolate the charge transfer event ( $-3 \rightarrow -2$ ) as coming from dynamics involving only two individual orbitals. For this reason, it is not surprising that, in order to obtain an accurate description of charge transfer, we must include the configurations:  $|\Phi_{hh}^{l+1}\rangle$  and  $|\Phi_{hh-1}^{\parallel}\rangle$ .

## V. CONCLUSION AND FUTURE DIRECTIONS

In conclusion, we have studied the two-site Anderson impurity model problem representing a multielectronic molecule sitting near a metal surface. After comparing the impurity population results for different CI methods, we find that  $CI(N-1, N-1)$  and  $CI(N-1, N+1)$  results match with the exact NRG results very well. Moreover, as far as the total energy is concerned,  $CI(N-1, N-1)$  (which is a relatively small CI matrix) often recovers more correlation energy than does  $CI(N_{ov}, 1)$  (which is a relatively large CI matrix)—this statement holds rigorously in the plateau region where the impurities have 3 electrons. This finding highlights the importance of corrections from doubly excited configurations. Another key conclusion is that  $CI(N-1, N-1)$  and  $CI(N-1, N+1)$  will differ strongly in the small limit of  $t_d = 0.02$ , where an *open shell singlet* can appear with 2 electrons on the impurities. In this limit, only  $CI(N-1, N+1)$  recovers correlation effects on the impurity population very well; furthermore, the method works in a robust fashion for all regimes tested so far (in terms of the intramolecular coupling strength  $t_d$  and the on-site energy difference between impurity site 2 and impurity site 1  $\Delta\varepsilon_d \equiv \varepsilon_{d2} - \varepsilon_{d1}$ ). Clearly, when describing electron-electron interactions for a molecule on a metal surface, accurate approximations are possible (though we still need to learn more about which approximation to choose and when).

Now, considering the minimal cost of a CAS(2,2) calculation and the moderate cost of a small CI calculation, combined with the possibility for quite reasonable accuracy when describing an impurity, the next step is to apply the present study within an *ab initio* DFT framework. Given that DFT can account reasonably well for dynamic correlation, one would hope that combining DFT with configuration interaction methods should describe both dynamical correlation and static correlation. Indeed, modern density functional theory is making progress as far as calculating excited state properties using Jacob's ladder of DFT (LSD, GGA, meta-GGA, hyper-GGA, and generalized RPA).<sup>83</sup> Thus, in the end, if DFT can be successfully merged with CI methods at a *metal-molecule interface* in a stable and efficient manner (and retain accuracy), there is the exciting possibility of simulating adiabatic and nonadiabatic chemical reaction processes near metal surfaces, including charge transfer processes, bond making processes, and bond breaking processes.

## ■ ASSOCIATED CONTENT

### Supporting Information

The Supporting Information is available free of charge at <https://pubs.acs.org/doi/10.1021/acs.jpcc.0c08750>.

Discussion on electron transfer in terms of configurations and the UHF broken symmetry approach (PDF)

## ■ AUTHOR INFORMATION

### Corresponding Author

Joseph Subotnik – Department of Chemistry, University of Pennsylvania, Philadelphia, Pennsylvania 19104, United

States; Phone: +1 (215) 746-7078; Email: [subotnik@sas.upenn.edu](mailto:subotnik@sas.upenn.edu)

## Authors

**Junhan Chen** – Department of Chemistry, University of Pennsylvania, Philadelphia, Pennsylvania 19104, United States; [orcid.org/0000-0003-4843-6324](https://orcid.org/0000-0003-4843-6324)

**Zuxin Jin** – Department of Chemistry, University of Pennsylvania, Philadelphia, Pennsylvania 19104, United States

**Wenjie Dou** – Department of Chemistry, University of California Berkeley, Berkeley, California 94720, United States

Complete contact information is available at:  
<https://pubs.acs.org/10.1021/acs.jpcc.0c08750>

## Notes

The authors declare no competing financial interest.

## ACKNOWLEDGMENTS

This work was supported by the U.S. Air Force Office of Scientific Research (USAFOSR) under Grant Nos. FA9550-18-1-0497 and FA9550-18-1-0420. We also thank the DoD High Performance Computing Modernization Program for computer time.

## REFERENCES

- (1) Bünermann, O.; Jiang, H.; Dorenkamp, Y.; Kandratsenka, A.; Janke, S. M.; Auerbach, D. J.; Wodtke, A. M. Electron-hole pair excitation determines the mechanism of hydrogen atom adsorption. *Science* **2015**, *350*, 1346–1349.
- (2) Morin, M.; Levinos, N.; Harris, A. Vibrational energy transfer of CO/Cu (100): Nonadiabatic vibration/electron coupling. *J. Chem. Phys.* **1992**, *96*, 3950–3956.
- (3) Huang, Y.; Rettner, C. T.; Auerbach, D. J.; Wodtke, A. M. Vibrational promotion of electron transfer. *Science* **2000**, *290*, 111–114.
- (4) Marcus, R. A. On the theory of oxidation-reduction reactions involving electron transfer. I. *J. Chem. Phys.* **1956**, *24*, 966–978.
- (5) Hush, N. Adiabatic theory of outer sphere electron-transfer reactions in solution. *Trans. Faraday Soc.* **1961**, *57*, 557–580.
- (6) Levich, V. G.; Dogonadze, R. R. An adiabatic theory of electron processes in solutions. *Dokl. Akad. Nauk* **1960**, 158–161.
- (7) Cukier, R. I.; Nocera, D. G. Proton-coupled electron transfer. *Annu. Rev. Phys. Chem.* **1998**, *49*, 337–369.
- (8) Jortner, J.; Bixon, M.; Langenbacher, T.; Michel-Beyerle, M. E. Charge transfer and transport in DNA. *Proc. Natl. Acad. Sci. U. S. A.* **1998**, *95*, 12759–12765.
- (9) Dou, W.; Subotnik, J. E. Nonadiabatic Molecular Dynamics at Metal Surfaces. *J. Phys. Chem. A* **2020**, *124*, 757–771.
- (10) Shenvi, N.; Roy, S.; Tully, J. C. Nonadiabatic dynamics at metal surfaces: Independent- electron surface hopping. *J. Chem. Phys.* **2009**, *130*, 174107.
- (11) Dou, W.; Subotnik, J. E. A broadened classical master equation approach for nonadiabatic dynamics at metal surfaces: Beyond the weak molecule-metal coupling limit. *J. Chem. Phys.* **2016**, *144*, No. 024116.
- (12) Jin, Z.; Subotnik, J. E. Nonadiabatic dynamics at metal surfaces: fewest switches surface hopping with electronic relaxation. *arXiv* **2020**; arXiv:2009.11261.
- (13) Dunning, T. H., Jr Gaussian basis sets for use in correlated molecular calculations. I. The atoms boron through neon and hydrogen. *J. Chem. Phys.* **1989**, *90*, 1007–1023.
- (14) Baer, M. *Theory of chemical reaction dynamics*; CRC: 1985; Vol. 3.
- (15) Liu, B. Classical barrier height for  $H + H_2 \rightarrow H_2 + H$ . *J. Chem. Phys.* **1984**, *80*, 581–581.
- (16) Nesbet, R. Approximate Hartree-Fock calculations for the hydrogen fluoride molecule. *J. Chem. Phys.* **1962**, *36*, 1518–1533.
- (17) Herzberg, G. *Molecular spectra and molecular structure. Vol. 1: Spectra of diatomic molecules*, 2nd ed.; Van Nostrand Reinhold: New York, 1950.
- (18) Roothaan, C. C. J.; Kelly, P. S. Accurate analytical self-consistent field functions for atoms. III. The  $1s^2 2s^m 2p^n$  states of nitrogen and oxygen and their ions. *Phys. Rev.* **1963**, *131*, 1177.
- (19) Moore, C. E. *Atomic energy levels as derived from analysis of optical spectra: 1H-23V*; US Government Printing Office: 1949; Vol. 1.
- (20) Sasaki, F.; Yoshimine, M. Configuration-interaction study of atoms. II. Electron affinities of B, C, N, O, and F. *Phys. Rev. A: At., Mol., Opt. Phys.* **1974**, *9*, 26.
- (21) Elder, F. A.; Villarejo, D.; Inghram, M. G. Electron affinity of oxygen. *J. Chem. Phys.* **1965**, *43*, 758–759.
- (22) Gräfenstein, J.; Cremer, D. Can density functional theory describe multi-reference systems? Investigation of carbenes and organic biradicals. *Phys. Chem. Chem. Phys.* **2000**, *2*, 2091–2103.
- (23) Imada, M.; Fujimori, A.; Tokura, Y. Metal-insulator transitions. *Rev. Mod. Phys.* **1998**, *70*, 1039.
- (24) Cao, Y.; Fatemi, V.; Demir, A.; Fang, S.; Tomarken, S. L.; Luo, J. Y.; Sanchez-Yamagishi, J. D.; Watanabe, K.; Taniguchi, T.; Kaxiras, E.; et al. Correlated insulator behaviour at half-filling in magic-angle graphene superlattices. *Nature* **2018**, *556*, 80.
- (25) Kaneko, T.; Yunoki, S.; Millis, A. J. Charge stiffness and long-range correlation in the optically induced  $\eta$ -pairing state of the one-dimensional Hubbard model. *Physical Review Research* **2020**, *2*, No. 032027.
- (26) Cevolani, L.; Despres, J.; Carleo, G.; Tagliacozzo, L.; Sanchez-Palencia, L. Universal scaling laws for correlation spreading in quantum systems with short-and long-range interactions. *Phys. Rev. B: Condens. Matter Mater. Phys.* **2018**, *98*, No. 024302.
- (27) Han, Q.; Millis, A. Lattice energetics and correlation-driven metal-insulator transitions: The case of  $Ca_2RuO_4$ . *Phys. Rev. Lett.* **2018**, *121*, No. 067601.
- (28) Keshavarz, S.; Schött, J.; Millis, A. J.; Kvashnin, Y. O. Electronic structure, magnetism, and exchange integrals in transition-metal oxides: Role of the spin polarization of the functional in DFT+ U calculations. *Phys. Rev. B: Condens. Matter Mater. Phys.* **2018**, *97*, 184404.
- (29) Knizia, G.; Chan, G. K.-L. Density matrix embedding: A simple alternative to dynamical mean-field theory. *Phys. Rev. Lett.* **2012**, *109*, 186404.
- (30) Anderson, P. W. Localized magnetic states in metals. *Phys. Rev.* **1961**, *124*, 41.
- (31) Bulla, R.; Costi, T. A.; Pruschke, T. Numerical renormalization group method for quantum impurity systems. *Rev. Mod. Phys.* **2008**, *80*, 395.
- (32) Fu, W.; Sachdev, S. Numerical study of fermion and boson models with infinite-range random interactions. *Phys. Rev. B: Condens. Matter Mater. Phys.* **2016**, *94*, No. 035135.
- (33) Gull, E.; Millis, A. J.; Lichtenstein, A. I.; Rubtsov, A. N.; Troyer, M.; Werner, P. Continuous-time Monte Carlo methods for quantum impurity models. *Rev. Mod. Phys.* **2011**, *83*, 349.
- (34) Wouters, S.; Jiménez-Hoyos, C. A.; Sun, Q.; Chan, G. K.-L. A practical guide to density matrix embedding theory in quantum chemistry. *J. Chem. Theory Comput.* **2016**, *12*, 2706–2719.
- (35) Lee, S. J.; Welborn, M.; Manby, F. R.; Miller, T. F., III Projection-based wavefunction- in-DFT embedding. *Acc. Chem. Res.* **2019**, *52*, 1359–1368.
- (36) Bulik, I. W.; Scuseria, G. E.; Dukelsky, J. Density matrix embedding from broken symmetry lattice mean fields. *Phys. Rev. B: Condens. Matter Mater. Phys.* **2014**, *89*, No. 035140.
- (37) Bulik, I. W.; Chen, W.; Scuseria, G. E. Electron correlation in solids via density embedding theory. *J. Chem. Phys.* **2014**, *141*, No. 054113.
- (38) Klüner, T.; Govind, N.; Wang, Y. A.; Carter, E. A. Periodic density functional embedding theory for complete active space self-consistent field and configuration interaction calculations: Ground and excited states. *J. Chem. Phys.* **2002**, *116*, 42–54.

- (39) Sharifzadeh, S.; Huang, P.; Carter, E. Embedded configuration interaction description of CO on Cu (111): Resolution of the site preference conundrum. *J. Phys. Chem. C* **2008**, *112*, 4649–4657.
- (40) Libisch, F.; Huang, C.; Carter, E. A. Embedded correlated wavefunction schemes: Theory and applications. *Acc. Chem. Res.* **2014**, *47*, 2768–2775.
- (41) Newns, D. Self-consistent model of hydrogen chemisorption. *Phys. Rev.* **1969**, *178*, 1123.
- (42) Kaduk, B.; Kowalczyk, T.; Van Voorhis, T. Constrained density functional theory. *Chem. Rev.* **2012**, *112*, 321–370.
- (43) Ma, H.; Wang, W.; Kim, S.; Cheng, M.-H.; Govoni, M.; Galli, G. PyCDFT: A Python package for constrained density functional theory. *J. Comput. Chem.* **2020**, *41*, 1859–1867.
- (44) Behler, J.; Delley, B.; Reuter, K.; Scheffler, M. Nonadiabatic potential-energy surfaces by constrained density-functional theory. *Phys. Rev. B: Condens. Matter Mater. Phys.* **2007**, *75*, 115409.
- (45) Souza, A.; Rungger, I.; Pemmaraju, C.; Schwingenschlögl, U.; Sanvito, S. Constrained-DFT method for accurate energy-level alignment of metal/molecule interfaces. *Phys. Rev. B: Condens. Matter Mater. Phys.* **2013**, *88*, 165112.
- (46) Gavnholt, J.; Olsen, T.; Englund, M.; Schiøtz, J.  $\Delta$  self-consistent field method to obtain potential energy surfaces of excited molecules on surfaces. *Phys. Rev. B: Condens. Matter Mater. Phys.* **2008**, *78*, No. 075441.
- (47) Roos, B. O.; Taylor, P. R.; Sigbahn, P. E. A complete active space SCF method (CASSCF) using a density matrix formulated super-CI approach. *Chem. Phys.* **1980**, *48*, 157–173.
- (48) Schmidt, M. W.; Gordon, M. S. The construction and interpretation of MCSCF wavefunctions. *Annu. Rev. Phys. Chem.* **1998**, *49*, 233–266.
- (49) Pauncz, R. *The symmetric group in quantum chemistry*; CRC Press: 1995.
- (50) Snyder, J. W.; Parrish, R. M.; Martinez, T. J.  $\alpha$ -CASSCF: an efficient, empirical correction for SA-CASSCF to closely approximate MS-CASPT2 potential energy surfaces. *J. Phys. Chem. Lett.* **2017**, *8*, 2432–2437.
- (51) Olsen, J. The CASSCF method: A perspective and commentary. *Int. J. Quantum Chem.* **2011**, *111*, 3267–3272.
- (52) Chan, G. K.-L.; Sharma, S. The density matrix renormalization group in quantum chemistry. *Annu. Rev. Phys. Chem.* **2011**, *62*, 465–481.
- (53) Andersson, K.; Malmqvist, P.-Å.; Roos, B. O. Second-order perturbation theory with a complete active space self-consistent field reference function. *J. Chem. Phys.* **1992**, *96*, 1218–1226.
- (54) Zgid, D.; Gull, E.; Chan, G. K.-L. Truncated configuration interaction expansions as solvers for correlated quantum impurity models and dynamical mean-field theory. *Phys. Rev. B: Condens. Matter Mater. Phys.* **2012**, *86*, 165128.
- (55) Gdanitz, R. J.; Ahlrichs, R. The averaged coupled-pair functional (ACPF): A size-extensive modification of MR CI (SD). *Chem. Phys. Lett.* **1988**, *143*, 413–420.
- (56) Lie, G. C.; Clementi, E. Study of the electronic structure of molecules. XXI. Correlation energy corrections as a functional of the Hartree-Fock density and its application to the hydrides of the second row atoms. *J. Chem. Phys.* **1974**, *60*, 1275–1287.
- (57) Lie, G. C.; Clementi, E. Study of the electronic structure of molecules. XXII. Correlation energy corrections as a functional of the Hartree-Fock type density and its application to the homonuclear diatomic molecules of the second row atoms. *J. Chem. Phys.* **1974**, *60*, 1288–1296.
- (58) Miehlich, B. B.; Stoll, H.; Savin, A. A correlation-energy density functional for multi-determinantal wavefunctions. *Mol. Phys.* **1997**, *91*, 527–536.
- (59) Grimme, S. Density functional calculations with configuration interaction for the excited states of molecules. *Chem. Phys. Lett.* **1996**, *259*, 128–137.
- (60) Grimme, S.; Waletzke, M. A combination of Kohn–Sham density functional theory and multi-reference configuration interaction methods. *J. Chem. Phys.* **1999**, *111*, 5645–5655.
- (61) Moscardó, F.; San-Fabián, E. Density-functional formalism and the two-body problem. *Phys. Rev. A: At, Mol, Opt. Phys.* **1991**, *44*, 1549.
- (62) Moscardó, F.; Muñoz-Fraile, F.; Pérez-Jiménez, A. J.; Pérez-Jordá, J. M.; San-Fabián, E. Improvement of multiconfigurational wave functions and energies by correlation energy functionals. *J. Phys. Chem. A* **1998**, *102*, 10900–10902.
- (63) Abia, L.; Pérez-Jordá, J.; San-Fabian, E. Mono and multi-configurational wave functions with DFT correlation energy: the case of fluorine. *J. Mol. Struct.: THEOCHEM* **2000**, *528*, 59–64.
- (64) Gräfenstein, J.; Cremer, D. Development of a CAS-DFT method covering non-dynamical and dynamical electron correlation in a balanced way. *Mol. Phys.* **2005**, *103*, 279–308.
- (65) Pijeau, S.; Hohenstein, E. G. Improved complete active space configuration interaction energies with a simple correction from density functional theory. *J. Chem. Theory Comput.* **2017**, *13*, 1130–1146.
- (66) Li Manni, G.; Carlson, R. K.; Luo, S.; Ma, D.; Olsen, J.; Truhlar, D. G.; Gagliardi, L. Multiconfiguration pair-density functional theory. *J. Chem. Theory Comput.* **2014**, *10*, 3669–3680.
- (67) Ghosh, S.; Sonnenberger, A. L.; Hoyer, C. E.; Truhlar, D. G.; Gagliardi, L. Multiconfiguration pair-density functional theory outperforms Kohn–Sham density functional theory and multireference perturbation theory for ground-state and excited-state charge transfer. *J. Chem. Theory Comput.* **2015**, *11*, 3643–3649.
- (68) Hoyer, C. E.; Ghosh, S.; Truhlar, D. G.; Gagliardi, L. Multiconfiguration pair-density functional theory is as accurate as CASPT2 for electronic excitation. *J. Phys. Chem. Lett.* **2016**, *7*, 586–591.
- (69) Gagliardi, L.; Truhlar, D. G.; Li Manni, G.; Carlson, R. K.; Hoyer, C. E.; Bao, J. L. Multiconfiguration pair-density functional theory: A new way to treat strongly correlated systems. *Acc. Chem. Res.* **2017**, *50*, 66–73.
- (70) Peng, W.-T.; Fales, B. S.; Shu, Y.; Levine, B. G. Dynamics of recombination via conical intersection in a semiconductor nanocrystal. *Chemical Science* **2018**, *9*, 681–687.
- (71) In principle, of course, for an exact calculation in the condensed phase, the number of virtual orbitals should be infinite; nevertheless, for the present calculations, we let  $N$  be the total number of atomic basis functions.
- (72) As far as generating parameters for this model using ab initio techniques, one can readily estimate  $t_{ij}$ ,  $E_{ij}$ , and  $E_k$  from the one-electron KS Hamiltonian.  $U$  is harder to estimate rigorously with standard DFT calculation; Voorhis *et al.* have argued that  $U$  can be estimated by constrained DFT (CDFT)<sup>42</sup> by fitting the parabolic nature of the curve  $\Delta E$  vs.  $\Delta N_{\text{tot}}$  (since the change in total energy should change quadratically with respect to the change in the number of electrons in a  $+U$  model).
- (73) Marzari, N.; Vanderbilt, D. Maximally localized generalized Wannier functions for composite energy bands. *Phys. Rev. B: Condens. Matter Mater. Phys.* **1997**, *56*, 12847.
- (74) Marzari, N.; Mostofi, A. A.; Yates, J. R.; Souza, I.; Vanderbilt, D. Maximally localized Wannier functions: Theory and applications. *Rev. Mod. Phys.* **2012**, *84*, 1419.
- (75) Teh, H.-H.; Subotnik, J. E. The simplest possible approach for simulating  $S_0$ - $S_1$  conical intersections with DFT/TDDFT—adding one doubly excited configuration. *J. Phys. Chem. Lett.* **2019**, *10*, 3426–3432.
- (76) In truth, the eigenspectrum forms a quasi-continuum and the energies of the four impurity related orbitals  $\{\psi_{h-1}, \psi_h, \psi_i, \psi_{h+1}\}$  are embedded within the bath orbitals. In other words,  $\psi_h$  is the highest occupied orbital in the impurity space but does not necessarily reside at the Fermi surface.
- (77) Coulson, C. A.; Fischer, I. XXXIV. Notes on the molecular orbital treatment of the hydrogen molecule. *London, Edinburgh, and Dublin Philosophical Magazine and Journal of Science* **1949**, *40*, 386–393.
- (78) Note that we do not report exact NRG results, as the NRG procedure produces a total energy that depends on the discretization procedure and is not meaningful.
- (79) Unfortunately, the usefulness of the latter is not clear. While the total energy of the ground state is meaningful on the basis of a variational procedure, the meaning of an excited state energy is less clear

as one expects a continuum of excited state energies to appear just above the ground state energy. In other words, even though excited states can be important or crucial when they participate in the dynamics of a given process, the exact energy belonging to a single excited state need not necessarily be important.

(80) For the curious reader, the difference in ground state energy between  $CI(1,N-1)$  and  $CI(N-1,N-1)$  is very small away from the crossing point, and can reach a modest 0.0008 at a crossing point.

(81) Jin, Z.; Dou, W.; Subotnik, J. E. Configuration interaction approaches for solving quantum impurity models. *J. Chem. Phys.* **2020**, *152*, No. 064105.

(82) Mott, N. Metal-insulator transition. *Rev. Mod. Phys.* **1968**, *40*, 677.

(83) Perdew, J. P.; Ruzsinszky, A.; Tao, J.; Staroverov, V. N.; Scuseria, G. E.; Csonka, G. I. Prescription for the design and selection of density functional approximations: More constraint satisfaction with fewer fits. *J. Chem. Phys.* **2005**, *123*, No. 062201.